

**PURDUE UNIVERSITY**  
**GRADUATE SCHOOL**  
**Thesis/Dissertation Acceptance**

This is to certify that the thesis/dissertation prepared

By Sunanda Koduvayur Parthasarathy

Entitled Transport studies of interaction effects in one and two dimensional hole systems

For the degree of Doctor of Philosophy

Is approved by the final examining committee:

Dr. Leonid P Rokhinson

Chair

Dr. Sergei Khlebnikov

Dr. Gabriele F Giuliani

Dr. Gabor Csathy

To the best of my knowledge and as understood by the student in the *Research Integrity and Copyright Disclaimer (Graduate School Form 20)*, this thesis/dissertation adheres to the provisions of Purdue University's "Policy on Integrity in Research" and the use of copyrighted material.

Approved by Major Professor(s): Leonid P Rokhinson

Approved by: Hisao Nakanishi

Head of the Graduate Program

09/24/2010

Date

**PURDUE UNIVERSITY  
GRADUATE SCHOOL**

**Research Integrity and Copyright Disclaimer**

Title of Thesis/Dissertation:

Transport studies of interaction effects in one and two dimensional hole systems

For the degree of Doctor of Philosophy

I certify that in the preparation of this thesis, I have observed the provisions of *Purdue University Teaching, Research, and Outreach Policy on Research Misconduct (VIII.3.1)*, October 1, 2008.\*

Further, I certify that this work is free of plagiarism and all materials appearing in this thesis/dissertation have been properly quoted and attributed.

I certify that all copyrighted material incorporated into this thesis/dissertation is in compliance with the United States' copyright law and that I have received written permission from the copyright owners for my use of their work, which is beyond the scope of the law. I agree to indemnify and save harmless Purdue University from any and all claims that may be asserted or that may arise from any copyright violation.

Sunanda Koduvayur Parthasarathy

Printed Name and Signature of Candidate

09/27/2010

Date (month/day/year)

\*Located at [http://www.purdue.edu/policies/pages/teach\\_res\\_outreach/viii\\_3\\_1.html](http://www.purdue.edu/policies/pages/teach_res_outreach/viii_3_1.html)

TRANSPORT STUDIES OF INTERACTION EFFECTS IN ONE AND TWO  
DIMENSIONAL HOLE SYSTEMS

A Dissertation

Submitted to the Faculty

of

Purdue University

by

Sunanda Koduvayur Parthasarathy

In Partial Fulfillment of the

Requirements for the Degree

of

Doctor of Philosophy

December 2010

Purdue University

West Lafayette, Indiana

To my two and four legged family

## ACKNOWLEDGMENTS

I would first like to thank my advisor Prof. Leonid Rokhinson to whom I owe practically everything I now know in experimental physics. Thanks Leonid, for being generous with your time and teaching me the tricks of the trade.

Many thanks to my committee members. To Prof. Gabriele F Giuliani for offering two very enjoyable classes and for always pushing me to get my fundamentals right. Prof. Sergei Khlebnikov for patiently answering my incessant questions in Statistical Physics and for helping me understand the results of my experiments. I greatly appreciate Prof. Gabor Csathy's constant support in and outside of the lab. Thanks for being so generous with your equipment and letting us use your fridge for our experiments on stripe phases.

Special thanks are due to Prof. Yuli Lyanda Geller for his extended theory that helped us interpret the results of our stripe experiments. I thank Prof. Michael Manfra, Prof. Loren Pfeiffer and Prof. Ken West for all the high quality samples that were measured in this thesis.

I thank the Department of Physics and the many lovely people here for their support during the last six years. Thanks to Prof. Anant Ramdas for being my first advisor at Purdue. I will cherish memories of our fun times at your place and our interesting corridor conversations. Thanks to Keith Schmitter for taking care of the liquefier and obliging my never-ending requests for Helium, always with a smile. Thanks to Mark Smith for helping me out with various electrical and electronic problems. Thanks to Sandy Formica, Linda Paquay, Carol Buuck and Pamela Blakey for bailing me out of all the paperwork drudgery so many times. You are the best support staff in Purdue. I would also like to thank Emmanuel, our custodian, for always bringing cheer into the room.

Thanks to all the members of Women in Physics for building a supportive environment where I could share some of the challenges that come with being a woman physicist. Thanks to my labmates Mason, Alex and Lishan for making the work in the lab more interesting. Thanks to my colleagues Ashwani, Luis, Helin and Romaneh for making the basement less spooky. My best wishes to the newcomers Tzu-ging Lin and Nishshanka. It was great getting to know you guys and I hope you have as much fun as I did working in B-46.

Many thanks to all my friends at Purdue, especially Chandra and my social groups through Asha for Education and ICMAP.

Above all my deepest gratitude goes to my family. I thank Appa for instilling in me an interest in research and science and for being my most honest critic. Amma, thanks for putting up with all my tantrums and for your unconditional love and belief in me. I can't thank my sisters Sujatha and Shuba enough for being with me through every single moment and providing me with a safety net. Mouli, thanks for being the best brother I could ever wish for and always putting things in perspective for me. Ravi, I am lucky to have your constant love through the last 7 years and for life. Thanks for being such a great sounding board and for your understanding every time I had to choose work over our time together. Last but not the least, my heartfelt thanks to my four legged family Imho, Frodo, Daphne, Tucker and Grapes who taught me how to get my life priorities right.

## TABLE OF CONTENTS

	Page
LIST OF TABLES . . . . .	vii
LIST OF FIGURES . . . . .	viii
ABSTRACT . . . . .	x
1 INTRODUCTION . . . . .	1
1.1 Band structure of holes in bulk GaAs . . . . .	2
1.2 Quasi two dimensional hole systems . . . . .	2
1.2.1 Size quantization and quantization axis . . . . .	4
1.3 Spin-Orbit coupling in two dimensional systems . . . . .	4
1.4 Transport in two dimensional systems . . . . .	5
1.4.1 Density and mobility . . . . .	5
1.4.2 Shubnikov de Haas oscillations . . . . .	6
1.5 Conductance quantization in 1D channels . . . . .	6
1.6 Quantum Hall Effect . . . . .	9
1.6.1 Fractional Quantum Hall Effect . . . . .	10
1.6.2 Nematic phases at high Landau levels : $N > 1$ . . . . .	11
2 DEVICE FABRICATION AND EXPERIMENTAL SETUP . . . . .	15
2.1 Heterostructures . . . . .	15
2.1.1 Si-doped GaAs/AlGaAs . . . . .	16
2.1.2 C-doped GaAs/AlGaAs along (001) . . . . .	17
2.2 Nanofabrication . . . . .	17
2.3 Optical Lithography . . . . .	17
2.4 Electron Beam Lithography . . . . .	18
2.5 Local Anodic Oxidation- AFM lithography . . . . .	24
2.6 Experimental setup . . . . .	28
2.6.1 Dilution Refrigerator . . . . .	28
3 ANISOTROPIC MODIFICATION OF THE EFFECTIVE HOLE $g$ -FACTOR BY ELECTROSTATIC CONFINEMENT <sup>1</sup> . . . . .	31
3.1 Introduction: $g$ -factor of two dimensional hole systems . . . . .	31
3.2 Sample details and experimental observations . . . . .	32
3.3 Effect of in-plane magnetic field . . . . .	35

<sup>1</sup>S. P. Koduvayur, L. P. Rokhinson, D. C. Tsui, L. N. Pfeiffer, and K. W. West, “Anisotropic modification of the effective hole  $g$ -factor by electrostatic confinement”, Physical Review Letters 100, 126401 (2008);arXiv:0802.4271

	Page
3.4 Non-linear transport spectroscopy . . . . .	38
3.5 Effect of diamagnetic shift on $g$ -factor anisotropy . . . . .	42
3.6 Unusual qualitative behavior of “half-integer” plateaus . . . . .	43
3.7 Conclusion . . . . .	43
4 EFFECT OF STRAIN ON NEMATIC PHASES IN TWO DIMENSIONAL HOLES <sup>2</sup> . . . . .	45
4.1 Nematic phases in Quantum Hall systems . . . . .	45
4.2 Sample and Experimental setup details . . . . .	47
4.3 Effect of external uniaxial strain on nematic phases . . . . .	50
4.4 Strain-induced anisotropic Hartree-Fock energy for holes . . . . .	51
4.5 Internal strain in GaAs/AlGaAs heterostructure caused by built in electric field . . . . .	58
4.6 Conclusion . . . . .	60
LIST OF REFERENCES . . . . .	62
VITA . . . . .	66

---

<sup>2</sup>Sunanda P. Koduvayur, Yuli Lyanda-Geller, Sergei Khlebnikov, Gabor Csathy, Michael J. Manfra, Loren N. Pfeiffer, Kenneth W. West, “Effect of strain on stripe phases in the Quantum Hall regime” arXiv:1005.3327v1

## LIST OF TABLES

Table	Page
3.1 Summary of experimental values used to extract $g^*$ for different energy levels for channel along $[1\bar{1}0]$ . . . . .	41
3.2 Summary of experimental values used to extract $\langle g^* \rangle$ for different energy levels for channel along $[\bar{2}33]$ . . . . .	41

## LIST OF FIGURES

Figure	Page
1.1 Band structure of GaAs . . . . .	3
1.2 Calculation of density from Shubnikov de Haas oscillations . . . . .	7
1.3 Quantized conductance for a Quantum Point Contact . . . . .	9
1.4 Schematic of Landau levels . . . . .	10
1.5 Stripe and bubble phases at higher Landau levels . . . . .	13
2.1 Mesa patterns used for optical lithography . . . . .	19
2.2 Process flow for fabricating devices using e-beam lithography . . . . .	20
2.3 Mesas used with e-beam lithography . . . . .	21
2.4 AFM micrograph and characterization of a sample fabricated using e-beam lithography . . . . .	23
2.5 Schematic of setup for AFM local anodic oxidation and characterization of a device fabricated using this technique . . . . .	25
2.6 Circuit for modulating tip bias voltage of an AFM . . . . .	27
2.7 Schematic of a dilution refrigerator . . . . .	30
3.1 AFM micrographs of QPCs fabricated on a sample and characterization at 4K . . . . .	33
3.2 Effect of in-plane field on conductance quantization of QPCs . . . . .	34
3.3 Conductance of QPC as a function of gate voltage for increasing magnetic field . . . . .	36
3.4 Conductance of QPC along $\bar{2}33$ as a function of gate voltage for increasing magnetic field . . . . .	37
3.5 Transconductance plots . . . . .	39
3.6 Summary of $g^*$ values obtained . . . . .	40
4.1 Density as a function of piezo actuator voltage and back gate voltage . . . . .	48
4.2 Magnetoresistance plots for various strain values . . . . .	49
4.3 Strain dependence of the anisotropic magnetoresistance of stripe phases . . . . .	51

4.4	(a) Ratio of isotropic and anisotropic parts of hole exchange potential (b) Band profile of the hole wafer studied (c) Model of HIGFET structure	57
-----	---	----

## ABSTRACT

Koduvayur Parthasarathy Sunanda Ph.D., Purdue University, December 2010. Transport studies of interaction effects in one and two dimensional hole systems. Major Professor: Leonid P Rokhinson.

Interest in hole systems has increased recently due to their potential applications in ‘spintronics’. They are characterized by stronger spin-orbit interaction and higher effective mass which is manifested in the form of stronger correlation effects. In this thesis, I present transport studies of hole systems grown on GaAs/AlGaAs heterostructures. The first project involves studies of anisotropy of spin-splitting in 1D channels by measuring conductance quantization of these channels as a function of gate voltage in the presence of an in-plane field. It is shown that the anisotropy of spin-splitting (characterized by the g-factor) in 1D channels is enhanced relative to the 2D anisotropy and is due to the crystalline anisotropy of spin-orbit interactions rather than due to lateral confinement.

In the second project, I study the effect of external strain on stripe phases in quantum Hall systems. The orientation of stripes is switched as a function of strain with stripes aligning along the direction of the large external uniaxial strain applied. I also present theoretical results that were obtained as part of a collaboration initiated due to the above mentioned experiments. The theoretical work attempts to understand the origin of preferential orientation of stripes along [110] for two dimensional hole gas grown along (001) GaAs. Hartree-Fock formalism is used to estimate anisotropic exchange interaction that explains orientation of stripes for different strain values. It is also shown that internal strains present in these heterostructures could be the reason for preferential orientation of stripes along [110] in these systems.

## 1. INTRODUCTION

There is probably no other discovery or invention in the 20th century that has changed man's life to an extent comparable to the discovery of the transistor [1]. Together with the follow up invention of the integrated chips in 1958/59 transistors have defined the present generation of electronics. Today's era of electronics depends on the miniaturization of solid state devices for improvement in speed and functionality. The progress towards incessant miniaturization is limited by the manifestation of quantum effects at these small scales. These unavoidable limitations on the conventional "top-down" approach has shifted the focus to the new paradigm of "bottom-up" nano-electronics.

The "bottom-up" approach explores the possibility of building scalable devices from precise atomically controllable building blocks. In the quest for ever increasing speed and efficiency, the journey of electronics took a new direction towards 'Spintronics'-an acronym for spin transport electronics, with the discovery of the giant magnetoresistive effect (GMR) [2, 3]. This new model changed the focus from electronic charge to spin as the basis for building devices. While initial demonstration of spintronics was done by controlling spins using external magnetic fields, it was soon realized that this was not viable for building a scalable architecture. Manipulation of spins using electric fields would be ideal for "on-chip" control of spins.

Spin-orbit(SO) coupling provides the fundamental link between spin and orbital degrees of freedom of an electron or hole, allowing manipulation of spins using electric fields. Since the proposal by Datta and Das [4] for a spin field effect transistor, interest in this field has increased tremendously. The strong spin-orbit interaction in hole systems has channelized this interest towards a better understanding of the complex valence band structure. In this thesis we study the effect of lateral confinement on spin splitting in two dimensional hole systems(chapter 3). Apart from applications in spintronics, hole systems provide a rich framework to understand many-body corre-

lation effects. The higher effective mass of holes, in comparison to electrons, results in comparably smaller kinetic energies and Fermi energies thus rendering the correlation effects more evident. In chapter 4 we try to better understand some correlation effects, like the nematic phases, found in two dimensional holes.

## 1.1 Band structure of holes in bulk GaAs

Transport properties of a semiconductor are characterized by its band structure or its dispersion relations: energy  $E_n(k)$  as a function of wave vector  $\mathbf{k}$ . Fig.1.1(a) shows a qualitative sketch of the band structure of bulk GaAs. While the conduction band has s-like symmetry and is parabolic, the valence band has p-like symmetry. Incorporation of SO terms in the Hamiltonian introduces a splitting in the valence band, with  $J = 3/2$  and  $J = 1/2$  states separated by the spin-orbit gap  $\Delta$ . At  $\Gamma$  point (center of the Brillouin zone) the spin orbit gap is 0.34eV in GaAs. Furthermore, the four fold degenerate  $J = 3/2$  hole bands further split at non-zero  $\mathbf{k}$ . These bands with  $J_z = \pm 3/2$  and  $J_z = \pm 1/2$  are called the heavy hole(HH) and light hole(LH) bands respectively. The distinction between heavy and light for these two bands comes from the difference in their effective masses.

## 1.2 Quasi two dimensional hole systems

In this work we study interaction effects in two dimensional hole gases(2DHG) and study spin splitting in one dimensional hole system which are fabricated from 2DHG. Thus it is very important to understand the effects of size quantization on the band structure of holes.

The most important effect of quantizing bulk GaAs into two dimensions is the lifting of the four fold degenerate  $J = 3/2$  hole bands at  $\Gamma = 0$ . The bands are split into heavy hole  $J_z = \pm 3/2$  states and light hole  $J_z = \pm 1/2$  states at  $k_{\parallel} = 0$ . The subband quantization introduces mixing between the HH and LH states leading to an anticrossing as shown in Fig.1.1(b). While the HH and LH states have

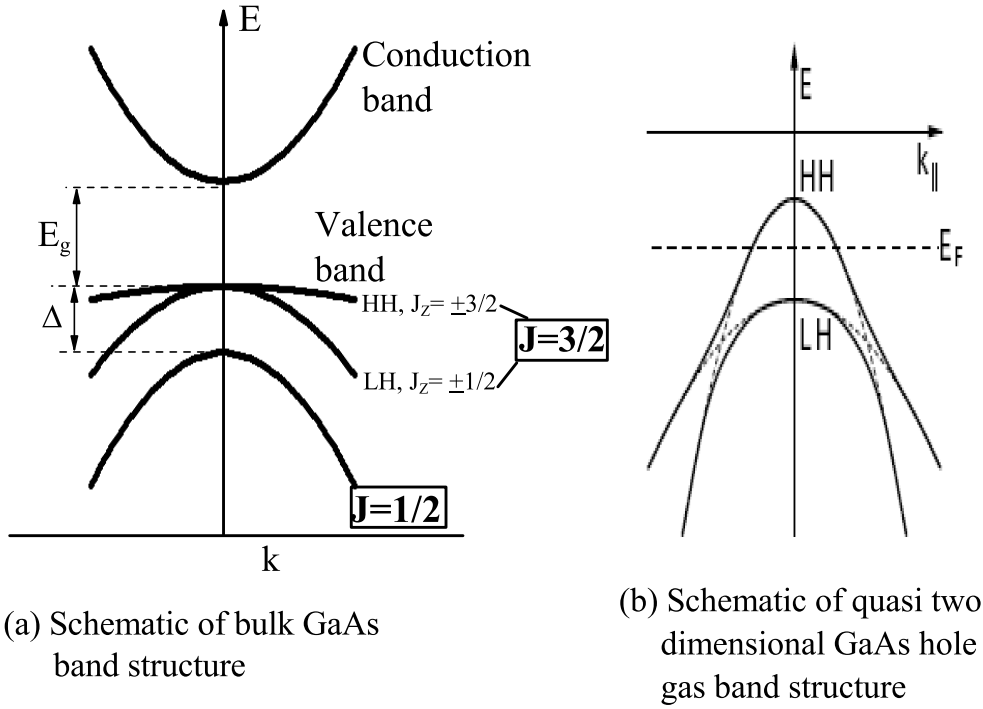


Figure 1.1. (a) Schematic of the band structure of bulk GaAs. The conduction band has s-like symmetry while the valence band has p-like symmetry.  $\Delta$  is the spin-orbit splitting and  $E_g$  is the energy gap of the material. (b) Schematic band structure for two dimensional GaAs. The degeneracy of the light hole(LH) and heavy hole(HH) bands is lifted at the center. LH-HH mixing causes anticrossings as shown by the dotted lines.  $E_F$  indicates the Fermi level.

larger and smaller effective masses, respectively, along the growth direction of the heterostructure, the roles are reversed in the plane of the 2DHG. That is, the HH(LH) states have smaller(larger) effective mass for motion in the plane of the 2DHG.

The spin orbit gap between the  $J = 1/2$  and  $J = 3/2$  bands is much larger than the splitting between the HH and LH splitting ( $\sim 10\text{meV}$ ). Thus transport physics is governed by the HH-LH bands in 2DHG. For typical densities in these heterostructures( $\sim 10^{11} \text{ cm}^{-2}$ ), the Fermi energy is of the order of  $2\text{meV}$ , thus in the low temperature limit only the top most heavy hole subband is occupied in 2DHG.

### 1.2.1 Size quantization and quantization axis

For 2DHG grown on (001) GaAs substrate with the orbital angular momentum quantized along the z-direction (the direction of growth of the heterostructure), spin orbit interaction locks the spins along the same direction. In the presence of an in-plane field, the g-factor, which quantifies the Zeeman splitting in the first order, is thus nearly zero [5, 6].

On the other hand for 2DHG grown along other low-symmetry directions like (311) this simple picture breaks down. Due to anisotropic orbital motion of the holes and the strong spin-orbit interactions present in these systems, the Zeeman splitting in the presence of an in-plane field, or equivalently the g-factor, becomes anisotropic with respect to the direction of the in-plane field relative to the crystallographic axes [7, 8].

In chapter 3 we see the effect of further quantization into one dimension for 2DHG grown along (311). Strong spin-orbit interaction enriches the picture further, giving us more degrees of freedom to fabricate one-dimensional devices.

### 1.3 Spin-Orbit coupling in two dimensional systems

Electrons and holes in semiconductors have a spin degeneracy at  $B = 0$ , i.e.  $E_{\uparrow}(\mathbf{k}) = E_{\downarrow}(\mathbf{k})$ . In the presence of an inversion-asymmetric potential, this degeneracy is lifted but the Kramer's degeneracy persists  $E_{\uparrow}(\mathbf{k}) = E_{\downarrow}(-\mathbf{k})$ . The inversion asymmetric potential could either be due to Bulk Inversion Asymmetry (BIA), wherein the crystal does not have a center of inversion (like GaAs and other Zinc-Blende structures) or could be due to Structural Inversion Asymmetry (SIA) which is essentially asymmetry of the confining potential. The BIA induced spin splitting is characterized by the Dresselhaus term and for 2D electrons is linear in  $k$ :  $H_D \propto (\sigma_x k_x - \sigma_y k_y)$ , where  $\sigma_x, \sigma_y$  are Pauli matrices. The proportionality constant depends on the band structure parameters of the crystal and spread of the wavefunction along the growth direction. The SIA induced spin splitting, also known as the Rashba term, is also linear in  $k$  for 2D electrons:  $H_R \propto (\sigma_x k_y - \sigma_y k_x)$ . Here the proportionality constant

depends on the electric field in the growth direction and other material parameters. In the case of 2D holes this picture of linear  $k$  terms changes due to the fact that the holes in the heavy hole band are spin  $3/2$  particles. The Dresselhaus and Rasha spin orbit terms are cubic in  $\mathbf{k}$

$$H_D \propto \sigma_+ p_- p_+ p_- + \sigma_- p_+ p_- p_+ \quad (1.1)$$

and

$$H_R \propto \sigma_+ p_-^3 - \sigma_- p_+^3. \quad (1.2)$$

where  $p_{\pm} = p_x \pm ip_y$  and  $\sigma_{\pm} = (\sigma_x \pm i\sigma_y)/2$ . Also in holes, the spin-orbit interactions are stronger as a result of their higher effective mass and the spin-splitting of the HH band is  $0.5\text{meV}$ .

## 1.4 Transport in two dimensional systems

### 1.4.1 Density and mobility

Two dimensional systems have the unique property that the density of states is independent of energy:

$$D = \frac{m^*}{\pi \hbar^2} \quad (1.3)$$

This gives a Fermi energy  $E_F = \frac{\pi \hbar^2}{m^*} n$  where  $n$  is the 2D density of holes(electrons). In the samples studied in this thesis, for  $n \sim 10^{11} \text{ cm}^{-2}$ , Fermi energy is  $\sim 2\text{meV}$  and Fermi wavelength given by  $\lambda_F = \sqrt{\frac{2\pi}{n}}$  is  $\sim 50 - 60\text{nm}$ . One of the important quantities in the magnetotransport studies of 2D semiconductors is the mobility. The semiclassical Drude theory gives mobility  $\mu = \frac{1}{ne\rho_s}$ , where  $\rho_s$  is the sheet resistivity which is proportional to the Hall resistance and the proportionality constant given by a geometrical factor:  $\rho_s = \frac{\pi R_{xx}}{ln2}$ . This is strictly valid only for low field where  $\omega_c \tau \ll 1$  with  $\omega_c = \frac{eB}{m^*}$ . The mobilities of the samples used in this thesis are  $0.4 \times 10^6 \text{ cm}^2/\text{Vs}$  (Chapter 3) and  $0.8 \times 10^6 \text{ cm}^2/\text{Vs}$  (Chapter 4), as measured at low temperatures. The density of these samples are measured from the low-field Shubnikov de Haas oscillations.

### 1.4.2 Shubnikov de Haas oscillations

A 2D electron(hole) gas in the presence of a perpendicular magnetic field has its energy quantized in a series of delta peaks, called the Landau levels(LL), which are separated by the cyclotron energy- $\hbar\omega_c$ . The sharp delta peaks broaden due to impurity scattering. The density of states at each LL is given by  $n_L = eB/h$ . As the field increases the density of states and the separation between the LLs increases. Thus, the filling factor which is the ratio  $\nu = \frac{n}{n_L} = \frac{hn}{eB}$ , decreases. As the field is increased, whenever the Fermi level lies in between two LLs, the density of states is a minimum, leading to both a minimum in resistivity ( $\rho_{xx}$ ) and conductivity( $\sigma_{xx}$ ). Thus the density of states and hence the resistivity oscillates with a period  $\propto 1/B$ . These oscillations are known as the Shubnikov de Haas oscillations. The density of the samples can be obtained experimentally using these oscillations ( $n = \nu eB/h$ ), as shown in Fig. 1.2. Beating due to the two spin-split subbands can be seen in the resistance as a function of magnetic field. The Fast Fourier Transform(FFT) of this data is shown in Fig. 1.2(b). FFT was done by a standard technique that makes use of a Hamming window. The densities of the samples used in this thesis were measured to be  $1.4 \times 10^{11} \text{cm}^{-2}$ (Chapter 3) and  $2.25 \times 10^{11} \text{cm}^{-2}$ (Chapter 4).

### 1.5 Conductance quantization in 1D channels

Conventionally resistivity of a sample is understood as the scattering of charge carriers with impurities in the sample. The average distance traveled by a charge carrier between scattering events is known as the mean free path. With the development of extremely clean materials, it is possible to fabricate quantum point contacts(QPC), whose widths are comparable to the Fermi wavelength of the carriers and much smaller than the mean free path. Transport in such devices where scattering is minimal is in the ballistic regime.

Classical expression of conductance in a point contact is given by  $G = \left(\frac{2e^2}{h}\right) \frac{k_F W}{\pi}$  where  $k_F$  is the Fermi wave vector and  $W$  is the width of the point contact. van

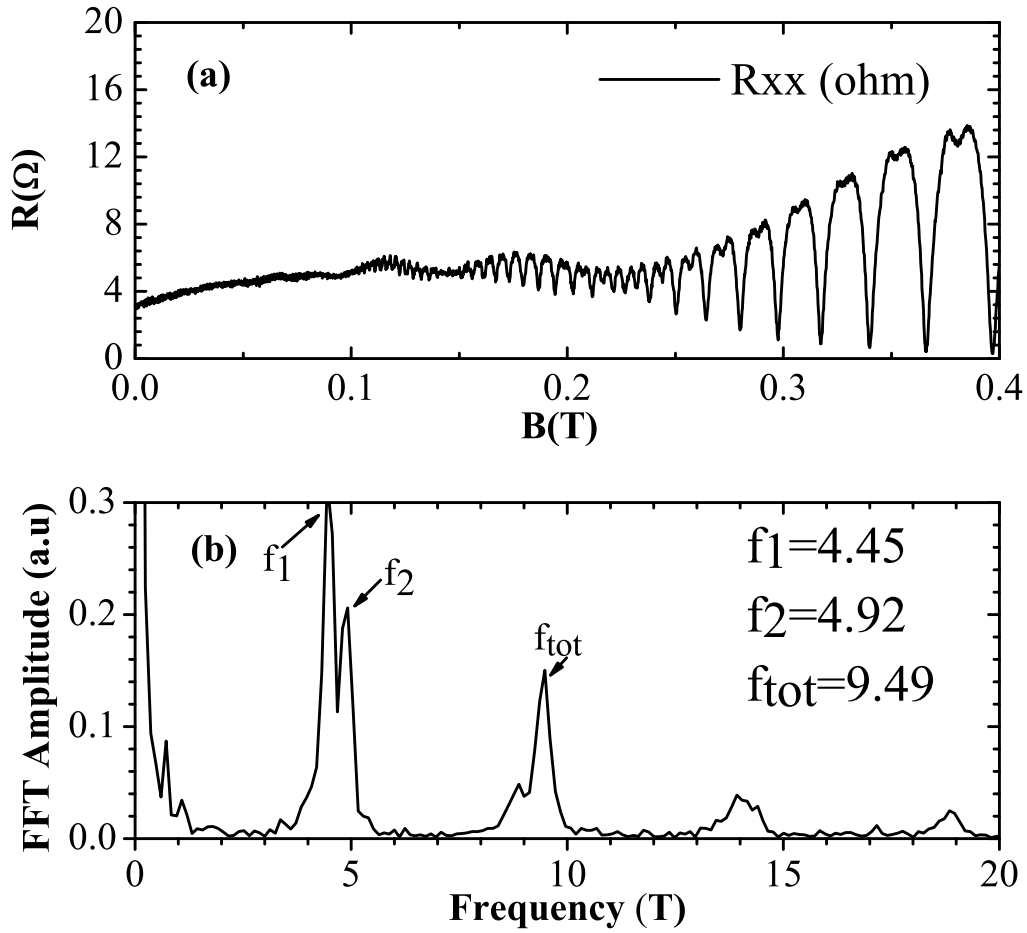


Figure 1.2. (a) Shubnikov de Haas oscillations in resistance of a 2D hole gas. Beating due to the two spin-split subbands is visible. (b) Fast Fourier Transform of data in (a) with magnetic field corresponding to the densities of the two subbands ( $f_1$  and  $f_2$ ) and the total density ( $f_{tot}$ ) are indicated.

Wees [9] (Fig. 1.3) and Wharam [10] first measured conductance of a QPC ( $\lambda_F \simeq W$ , where  $\lambda_F$  is the Fermi wavelength) fabricated in a 2D electron gas. Surprisingly they found that the conductance of the quantum point contact to be quantized in units of  $\frac{e^2}{h}$ .

Landauer and Buttiker [11,12] proposed the theory of conductance as transmission in quantum point contacts:  $G = \frac{2e^2}{h} T = \frac{2e^2}{h} \sum_{n,m=1}^N |t_{nm}|^2$ , where  $t$  is the transmission matrix,  $T$  is the total transmission and the sum is over all transverse modes in the QPC. A simplistic picture to understand this model would be to consider the QPC as a wave guide. There is an equipartition of current amongst all the modes at the Fermi level as the product of the group velocity and density of states is a constant for a 1D system. Each transverse mode in the QPC contributes  $2e^2/h$  (the factor 2 includes the spin degeneracy) to the conductance of the channel. If there are  $N$  modes at the Fermi level, this gives a conductance of  $G = N \frac{2e^2}{h}$ . As the width  $W$  of the QPC decreases, the number of transverse modes  $N \approx 2W/\lambda_F$ , in the QPC decreases, leading to a decrease in the conductance by a discrete quantum of  $2e^2/h$  or integer multiples of it.

While QPCs in electron systems have been rigorously researched from as early as the late 80s, first observation of quantized conductance in holes came only six years later [13–15] due to challenges in fabrication. Observation of clean conductance steps on par with those of electron systems is always a challenge in hole systems due to their higher effective mass which reduces the energy level spacing and the mean free path, making resolution of conductance plateaus and observation of ballistic transport more difficult. Fig. 1.3 shows conductance quantization for a QPC on a two dimensional electron(a) and hole(b) gas. Fig. 1.3(a) is from [9]. Note the opposite polarity of the gate voltage.

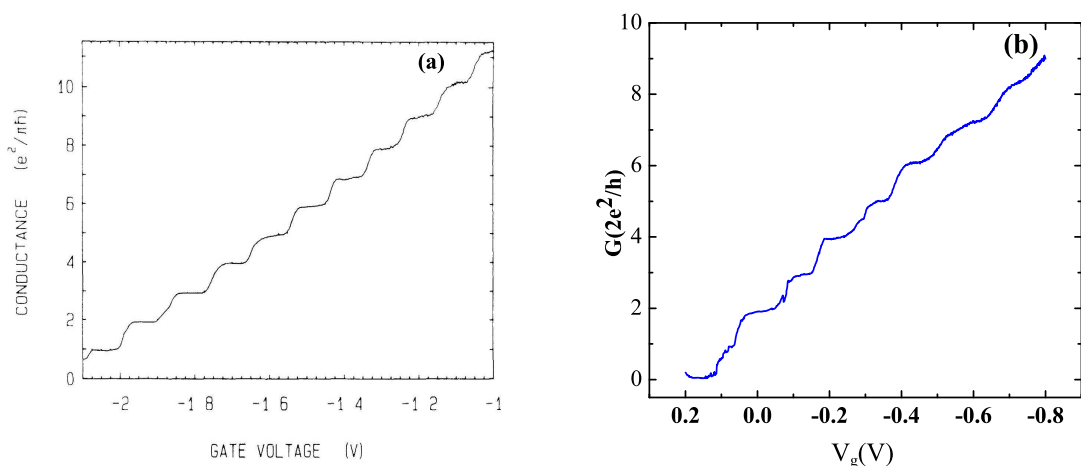


Figure 1.3. Conductance as a function of gate voltage for a Quantum Point Contact fabricated from (a) two dimensional electron gas and (b) two dimensional hole gas. (a) is taken from B.T.van Wees et. al. Phys. Rev. Lett. 60, 848850 (1988).

## 1.6 Quantum Hall Effect

Since its discovery in 1980, quantum Hall effect has opened a wide range of intriguing puzzles in low dimensional condensed matter physics. Klaus Von Klitzing measured the resistance of a two dimensional electron gas in the presence of perpendicular magnetic fields. It was found that the Hall conductivity was quantized in integer steps of  $\frac{2e^2}{h}$  as the density of electrons was changed, at a constant perpendicular field. Energy of a two dimensional electron system in the presence of a perpendicular magnetic field is quantized into discrete Landau levels :  $E = E_0 + (N + 1/2)\hbar\omega_c$  where  $\hbar\omega_c = \frac{\hbar eB}{m_c}$  is the cyclotron energy. As the density changes, the Fermi level steps through the various Landau levels. For the range of gate voltages when the Fermi level lies in the gap of localized states between the Landau levels, the conductivity is quantized at  $\frac{\nu e^2}{h}$ , where  $\nu$  is the filling fraction defined by  $\nu = \frac{nh}{eB}$  (Fig. 1.4). This exact quantization (accuracy of one part in a billion) of Hall resistance led to the definition

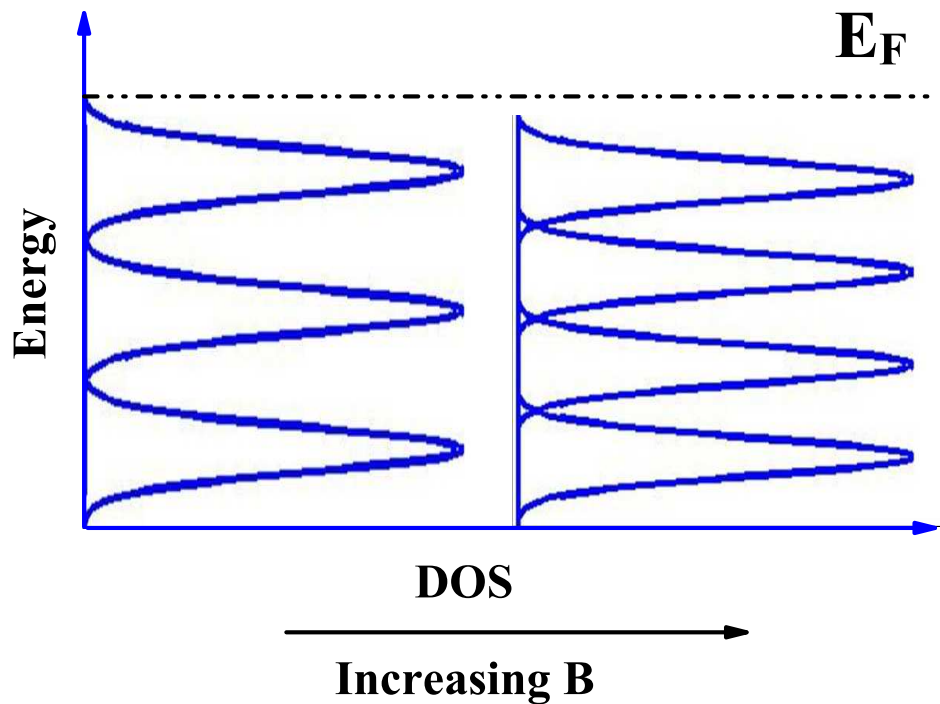


Figure 1.4. Schematic of two dimensional density of states (Landau Levels) in the presence of a perpendicular magnetic field. The separation between the Landau levels decreases as magnetic field  $B$  increases.

of a new standard of resistance :  $\frac{h}{e^2}$  known as the Klitzing constant. High precision measurements of the quantum Hall resistance also leads to the precise determination of the fine structure constant  $\alpha$  which is proportional to  $\frac{e^2}{h}$ .

### 1.6.1 Fractional Quantum Hall Effect

Theory had predicted that for the lowest LL,  $\nu < 1$ , the electrons would arrange themselves in a triangular lattice known as the Wigner solid. Soon after the experimental discovery of IQHE, Dan Tsui, Horst Stormer and Arthur Gossard observed another interesting feature while studying very clean two dimensional electron

gas formed at the interface of a GaAs/AlGaAs heterostructure. While measuring the Hall resistance they found new steps that were quantized at fractional multiples of the fundamental constant  $\frac{h}{2e^2}$ . The initial speculation was that this was an experimental evidence for the formation of the Wigner crystal. Interestingly enough the initial experiments showed steps at fractions with odd denominators. Most of the FQHE states were seen in the lowest two LLs,  $N=0$  and 1. It turned out that the Wigner crystal picture was not the correct explanation for the formation of the FQHE states. A year after the experimental observation of FQHE, Laughlin proposed a model based on fractionally charged quasiparticles which explained the presence of the odd-denominator fractionally quantized states. The ground state of the two dimensional quantum fluid of quasiparticles, known as the Laughlin liquid, is given by the Laughlin wavefunction [16]:

$$\Psi_m = \left\{ \prod_{i < j} (z_i - z_j)^m \right\} \exp\left(\frac{-1}{4} \sum_i |z_i|^2\right) \quad (1.4)$$

where  $z_i$  is the position of the  $i^{\text{th}}$  electron and is given by  $z = x + iy$ . Most of the FQHE states can be successfully explained using the composite fermion picture.

A few years later Willet et al made yet another surprising observation of an even denominator fractionally quantized state at filling fraction  $\nu = 5/2$ . The exact nature of this state is still under debate.

The field of quantum hall effect and fractional quantum hall effect has thus proved to be a fertile ground to understand correlation effects resulting in various novel quantum phases of matter, making it an extremely active field of research even after 28 years of its discovery.

### 1.6.2 Nematic phases at high Landau levels : $N > 1$

Before the experimental discovery of Quantum Hall Effect(QHE), [17] suggested that the two dimensional electron gas is unstable to the formation of a charge density wave. Much later it was proposed that CDWs should form the ground state for higher Landau levels,  $N > 1$  by both Fogler, Koulakov, Shklovski [18, 19] and Moessner,

Chalker [20]. [18, 19] predict that at half-fillings of higher LLs ( $N > 1$ ), a stripe phase of the CDW is formed which is made up of alternating strips of filled and empty states of the topmost LL. They also predicted that away from the half-filling this stripe phase develops into a triangular bubble phase, where 2 or more electrons occupy the triangular lattice sites (Fig. 1.5(a) and (b)).

Experimental evidence for the stripe phases came in the form of Anisotropic Magnetoresistance (AMR) observed at half-fillings of  $N > 1$  LLs in electrons [21, 22] and holes [23, 24]. The resistance was measured (for current predominantly flowing in the same direction i.e.  $R_{xx}$ ) along the principal axes of the 2D gas at half-filling of these levels. It was observed that it showed a peak or minimum depending on the axes. A characteristic plot of magnetotransport for a 2D GaAs hole gas grown along (001) is shown in Fig. 1.5(c). The difference between the red and blue curves is just the orientation of current and voltage contacts, which are perpendicular to each other and along the principal axes  $[110]$  and  $[1\bar{1}0]$  respectively. At  $\nu = 7/2$  resistance along  $[110]$  shows a minimum while resistance along  $[1\bar{1}0]$  shows a maximum. This difference in resistance is understood to be the consequence of transport being easier along the stripes compared to perpendicular to the stripes. The other salient experimental feature observed is the ‘satellite’ peaks on either side of half-filling (seen close to  $1/4$  fillings) that are separated from the peaks at half-filling by an insulating region.  $R_{xy}$  at these insulating regions is quantized to the nearby integer quantum hall state values and thus are called the Re-entrant Integer Quantum Hall Effect (RIQHE) states. The insulating RIQHE state can be interpreted as due to the disorder pinning of the bubble phase [25].

The consistent experimental feature observed in all of the above experiments has been the orientation of the stripe phases along  $[110]$  for 2D gas grown along (001) GaAs. In Chapter 4 of this thesis we try to understand the anisotropic interactions that orient stripes along  $[110]$  by applying external strain.

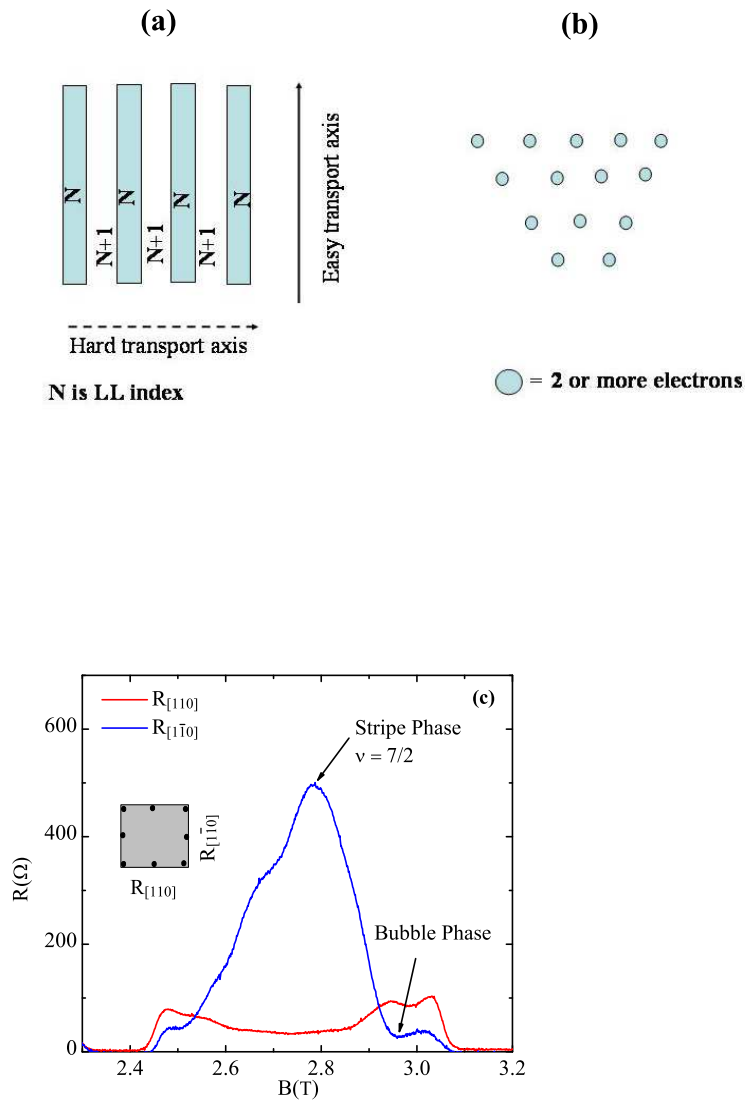


Figure 1.5. (a) Schematic of the formation of stripe faces at half-filling of  $N > 1$  LLs. (b) Schematic of formation of bubble phase away from half fillings for  $N > 1$ . (c) Characteristic magnetotransport data for a two dimensional hole system, showing the stripe phase at  $\nu = 7/2$  and the bubble phase close to it. The red and blue curves are resistance along the two perpendicular directions of the sample, as shown in the inset.

## Further Reading

I suggest here some references for a more detailed introduction to the topics covered in this thesis.

1. “Spin-Orbit coupling effects in Two-Dimensional electron and hole systems” by Roland Winkler. Springer Tracts in Modern Physics
2. “Introduction to mesoscopic physics” by Yoseph Imry. Oxford University Press
3. “The Quantum Hall Effect (Graduate Texts in contemporary physics/Maryland subseries)”-Edited by Richard E Prange and Steven Girvin
4. “Quantum Theory of the Electron Liquid” by Gabriele Giuliani and Giovanni Vignale. Cambridge University Press
5. “The Physics of Low-Dimensional Semiconductors” by John H Davies. Cambridge University Press

## 2. DEVICE FABRICATION AND EXPERIMENTAL SETUP

### 2.1 Heterostructures

The starting point for the devices fabricated in this work is a heterostructure made of GaAs and  $\text{Al}_x\text{Ga}_{1-x}\text{As}$ . The almost identical lattice constants of these two compounds leads to a final structure with no strain. The heterostructures in this work were grown by Loren Pfeiffer, Ken West and Michael Manfra in Bell Labs using Molecular Beam Epitaxy (MBE). The technique involves depositing monolayers of elements that constitute the heterostructure on the substrate, GaAs here. The chamber is under ultra high vacuum, resulting in molecules of the elements having very large mean free path so that they are not scattered until they hit the substrate or the walls of the chamber. Very clean interfaces can thus be realized, which in turn reduces impurity scattering and improves mobility of these heterostructures. The heterostructures used in this work are quantum wells of GaAs sandwiched between layers of AlGaAs. The important step in the growth of a heterostructure is the doping layer which provides the charge carriers. Modulation doping is a commonly used technique to reduce the scattering with donors. In this method the structure is doped remotely, away from the quantum well and the charge carriers migrate to the quantum well interface. The motion of charge carriers along the  $z$  direction (growth direction) is quantized. For our samples with densities  $\sim 10^{11} \text{ cm}^{-2}$  and well widths  $\sim 20 \text{ nm}$  only the lowest level is occupied. The charge carriers are free to move in the plane perpendicular to the growth direction, and this constitutes the two dimensional electron/hole gas. Samples in this work were made from two different heterostructures

grown along different crystallographic axes. The transport properties are also different thus making them suitable in different regimes of transport studies.

### 2.1.1 Si-doped GaAs/AlGaAs

With the increasing interest in hole GaAs/AlGaAs systems for their applications in spintronic devices and in the study of spin-orbit interactions, the quality and techniques of growth of these heterostructures also improved. The conventional technique of using Be-dopants along (001) orientation of GaAs resulted in high sample disorder limiting the highest mobilities achievable in two dimensional hole systems. Due to the engineering advantage of using a single source to grow both n-type and p-type GaAs wafers in the same Molecular Beam Epitaxy(MBE) chamber and a smaller diffusion constant, Si was chosen as the dopant. Along (311) Si is incorporated in the Arsenic site and acts as an acceptor. Sharper Si distribution made mobilities of the order of  $\sim 0.3-0.4 \cdot 10^6 \text{cm}^2/\text{Vs}$  achievable.

Due to the lower symmetry of wafers grown along (311) the band structure is more anisotropic (hence sometimes more interesting) than the band structure of wafers grown along (001). For 2D gas grown along (311) direction, the 2D plane is defined by the axes  $[1\bar{1}0]$  and  $[\bar{2}33]$ . The dispersion curves (energy versus in-plane wave vector) of some of the higher subbands are known to have a camel back structure with minima along the  $[1\bar{1}0]$  direction [26]. The  $[\bar{2}33]$  direction has corrugations (as a by-product of growth) which result in interface scattering leading to a mobility anisotropy in the plane of the 2D hole gas. Mobility along  $[\bar{2}33]$  can be higher by a factor of 2-4 than the mobility along  $[1\bar{1}0]$  [27]. These complications in the transport properties of this low symmetry growth direction lead to some rich physics which becomes apparent in our study of g-factor of holes using a quantum point contact in Chapter 3.

The use of atomic force microscope (AFM) lithography to make low dimension samples further restricts the design of heterostructures that could be used for our work. For efficient depletion of the 2D gas under the oxide layer, the 2DHG cannot

be deeper than 40nm from the surface [28]. Samples for the work on quantum point contacts have been made from heterostructure described in [15].

### 2.1.2 C-doped GaAs/AlGaAs along (001)

Further improvement (beyond  $0.3-0.4 \times 10^6 \text{ cm}^2/\text{Vs}$ ) in mobilities for structures grown along (311) is believed to be limited by the interface roughness scattering [29]. The plane of the 2D gas for growth along (001) is characterized by [110] and  $[1\bar{1}0]$  axes. The very low mobility anisotropy between  $[1\bar{1}0]$  and [110] ( 20%) makes certain transport experimental results (like our study of the nematic phases) easier to interpret. Recent improvement in fabrication techniques has led to mobilities  $\sim 10^6 \text{ cm}^2/\text{Vs}$  at a density of  $10^{11} \text{ cm}^{-2}$  [30].

Samples for the study of nematic phases were made from wafer fabricated with the heterostructure design described in [24](sample C).

## 2.2 Nanofabrication

A combination of various lithography techniques and etching methods are used to fabricate the nanodevices from the plain GaAs/AlGaAs heterostructures described above. We use three different kinds of lithography techniques to pattern the heterostructure depending on the length scale at which the sample is processed. The operating principles and the advantages and disadvantages of these techniques are given below.

## 2.3 Optical Lithography

We use optical lithography as a first step in device fabrication: to make circular mesa structures of radius  $10\mu\text{m}$ . This helps in making electrical contacts to the low dimensional devices which are then fabricated using AFM lithography/ e-beam lithography. All optical lithography in this work was done on the Suss MJB3 mask

aligner at the Birck Nanotechnology Center. Resolution of  $0.6 \mu\text{m}$  and alignment accuracies of  $1.0 \mu\text{m}$  can be achieved using this mask aligner. Fig. 2.1 shows the basic structure, at two magnifications, that was patterned for all the one dimensional devices used in this work. After cleaning the wafer with Trichloroethylene, Acetone and Isopropyl alcohol, AZ1518 photoresist(positive) is spun for 40 seconds at 6000 rpm. It is then pre baked at  $110^\circ\text{C}$  for 1 minute. The desired mask is then aligned with the wafer and exposed with UV light of wavelength 400nm. A solution of AZ 351 and DI water in the ratio 1:5 is used to develop the exposed areas. Photoresist is removed from those regions that were exposed with UV light. The wafer is then post-baked at  $90^\circ\text{C}$  for 30-60 min followed by wet etching using piranha etch :  $\text{H}_2\text{O}:\text{H}_2\text{SO}_4:\text{H}_2\text{O}_2$  in the ratio 1:8:1000 for 2 minutes. This gives trenches 100nm deep, which isolates regions of 2D hole gas at low temperatures(4K). Photoresist is then removed using acetone.

## 2.4 Electron Beam Lithography

E-beam lithography is the most common technique used to pattern nanodevices on a two dimensional electron/hole gas. It is versatile in the sense of bridging many length scales. The  $3\text{mm} \times 3\text{mm}$  mesa structures described in the previous section as well as the fine one dimensional devices that range between few tens of nanometers, both can be fabricated using this technique. While the devices made using e-beam lithography were not measured for this thesis due to other experimental constraints, considerable time and effort was spent in fine tuning the parameters and calibrating the lithography procedure. To that end, the basic procedure to fabricate low dimensional devices and rudimentary characterization of these devices is presented below.

The process flow for fabricating devices is shown in Fig. 2.2. Briefly, the sample is first cleaned using the standard three solvent procedure - Trichloroethylene, Acetone and Alcohol. E-beam positive photoresist, like the PMMA (4% solution of 950PMMA

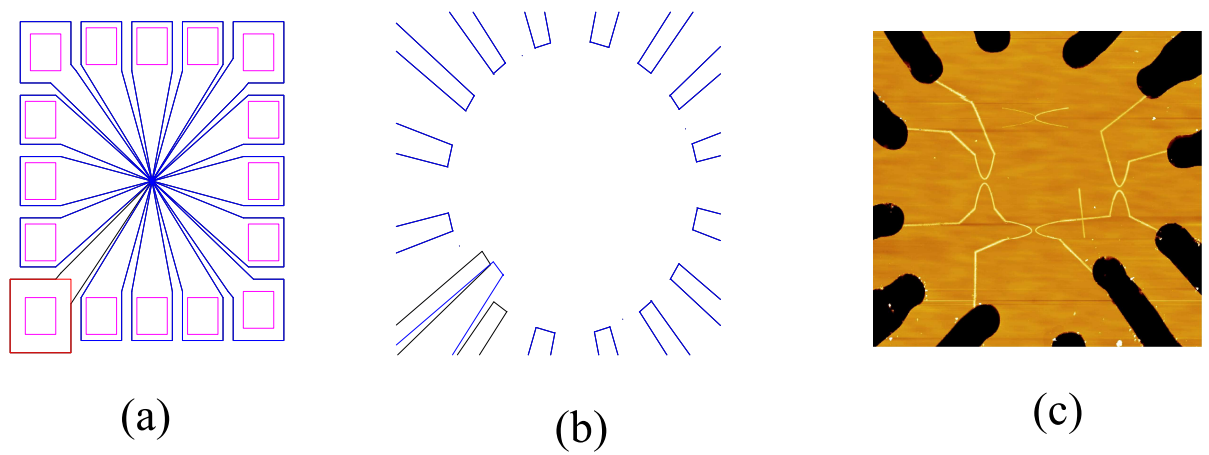


Figure 2.1. (a) 3mmx3mm mesa that are patterned onto the sample surface by optical lithography. Pink squares are the windows for the In/Zn contacts. The blue lines are the regions that are etched and hence isolates conducting regions of the 2D gas. (b) Central region of the mesa—a circular area of  $10\mu\text{m}$  radius, onto which devices are fabricated using AFM. (c) AFM micrograph of the central region of the sample. White lines are oxide lines that separate the 2D gas. The black regions are the etched out lines from the previous step of optical lithography.

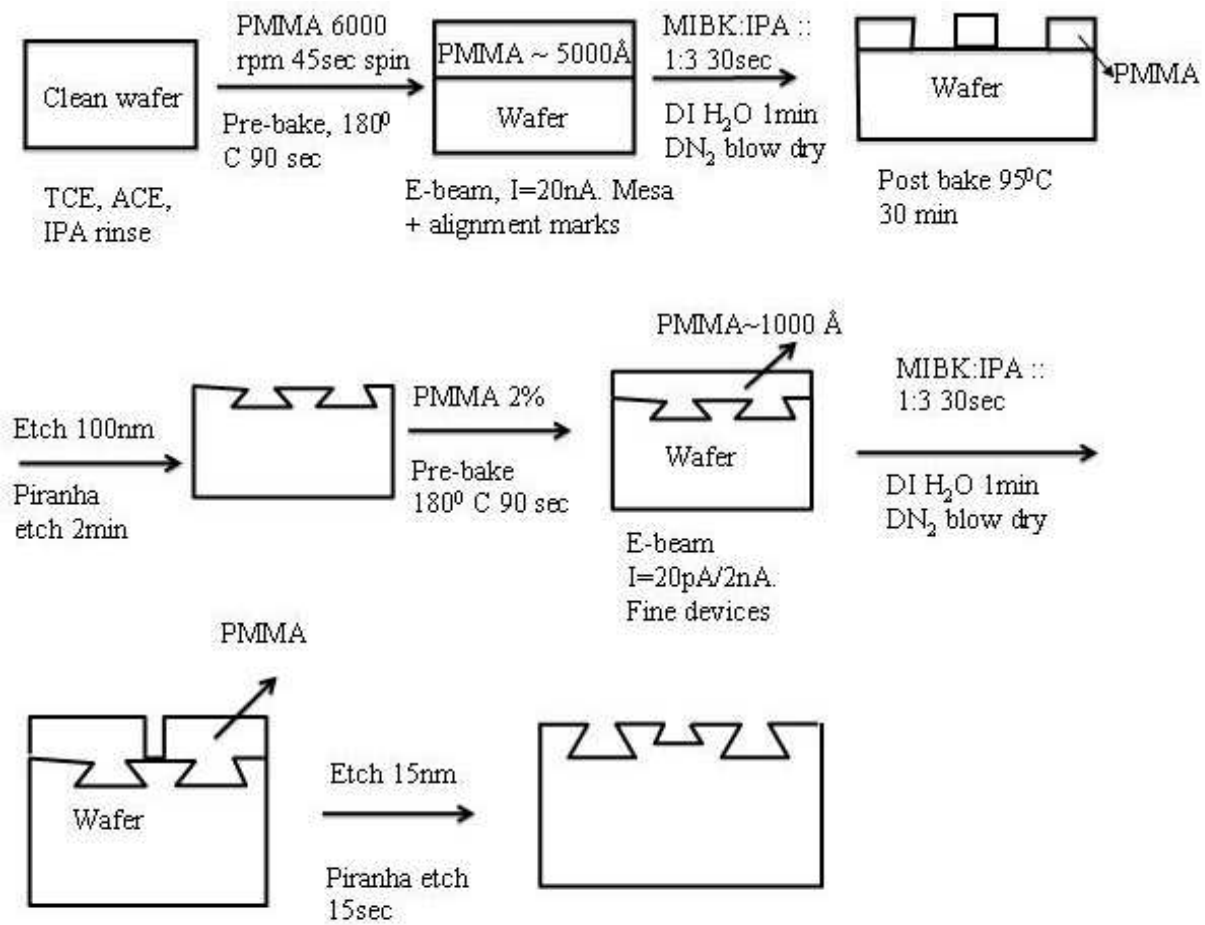


Figure 2.2. Process flow for fabricating mesa and fine one dimensional devices using e-beam lithography.

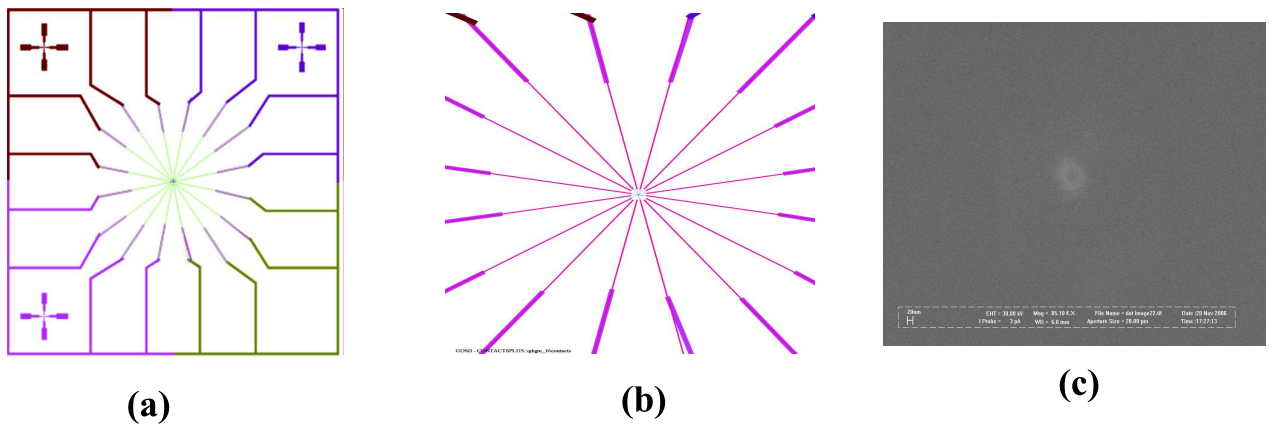


Figure 2.3. (a)  $3\text{mm} \times 3\text{mm}$  mesa pattern with alignment marks in the 3 corners of the square that is the first step in patterning using e-beam. (b) The second step of connecting lines (in pink) and fine devices (in blue) that are patterned after aligning. (c) Screen shot of a focussed beam at  $10\text{pA}$  for  $10\text{sec}$ .

in chlorobenzene)(Poly MethylMethAcrylate) is spun at 6000 rpm for 45 sec ( 5000 $\text{\AA}$ ). While thinner PMMA can be used for wet etching(it is crucial to have thick photoresist for evaporation of contact pads which is not described in this particular process flow) the exposure parameters presented below have been fine tuned for this thickness. The sample is then pre-baked at 180 $^{\circ}$  C for 90 sec. In the first exposure step, the 3mm $\times$ 3mm mesa, along with the alignment marks fig. 2.3(a) is written. The mesa pattern is then developed in a solution of MIBK:IPA :: 1:3 for 30 seconds. To stop the developing process, the sample is sprayed with DI water for  $\sim$  1min, followed by Dry N<sub>2</sub> blow dry. It is then post baked @ 95 $^{\circ}$ C for 30 min followed by etching similar to the process after optical lithography, described in previous section. The etched (100nm deep) regions (colored in fig. 2.3(a)(b)) separate areas of 2D gas. To write the finer devices the sample is spun with a thinner photoresist layer (PMMA 2% in Chlorobenzene) at 6000 rpm for 45sec and pre-baked as before. The sample is then aligned using the alignment markers. After alignment, the beam is focused at low current values of  $\sim$ 10pA, close to the central region ( $\sim$ 100nm away from the center) by burning spots (starting from 30 sec and successively reducing the time by 5-10 sec) followed by imaging the spots. It is important to get a well focussed beam before attempting to write the fine patterns. A well focussed beam has a spot(5-10sec) that is  $\sim$ 20-40nm in radius and is in the form of a doughnut. A snapshot of the focussed spot is shown in fig. 2.3(c). The finer patterns are then written at 15-20pA, and the lines that connect the fine device to the previously etched regions are written at 2nA (fig. 2.3(b)). The post processing is done similar to the previous step of writing a mesa, with the etching done only up to 20nm. Fig. 2.4(a) shows a nanodevice- a quantum dot with a quantum point contact as a sensor- that was fabricated with this technique. As can be seen in Fig. 2.4(b), the device shows good control with the side gates and the etched lines separate regions of 2D gas.

While this technique is versatile in being able to fabricate all length scales involved in the fabrication, it is not suitable for very shallow 2D systems as the damage caused to the surface due to the energetic e-beam is considerable.

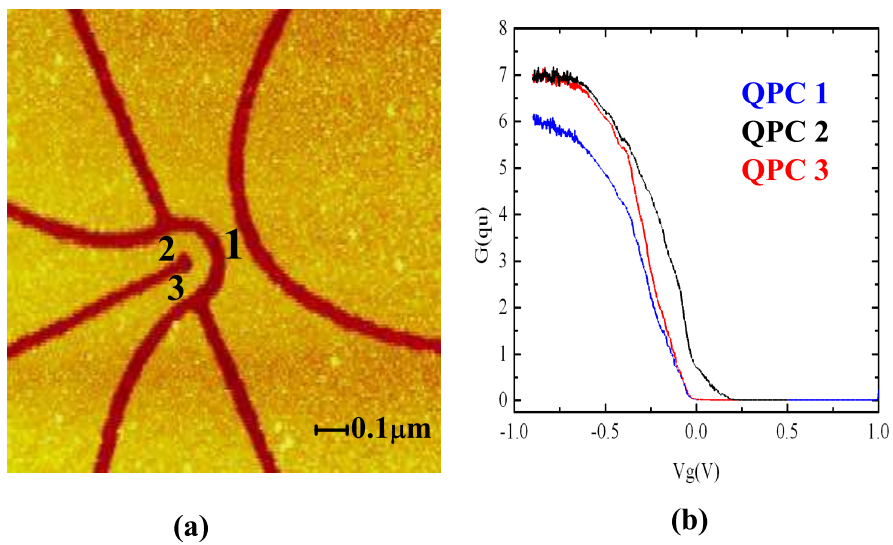
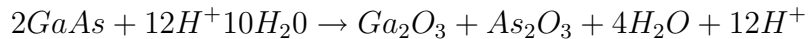


Figure 2.4. (a) AFM micrograph of a quantum dot device with a quantum point contact sensor fabricated using e-beam lithography. The different point contacts that can be probed are marked in black. (b) Conductance of the three quantum point contacts marked in (a) as a function of gate voltage at 4K (all the gates are ramped together)

## 2.5 Local Anodic Oxidation- AFM lithography

Atomic Force Microscope (AFM) lithography is a powerful tool in nanofabrication used to achieve nanometer scale resolution [31,32]. It scores over the widely used electron beam lithography technique by requiring lower energies and hence causing lesser damage to the semiconductor surface. It also has the advantage of post measurement tunability of the devices. AFM-local anodic oxidation (LAO) leads to sharper potential compared to the top gating technique and also eliminates leakage problems associated with low Schottky barriers in p-GaAs.

The procedure involves scanning a clean surface of the sample, that is grounded, with a negatively biased tip in a humid atmosphere, Fig. 2.5. We use a Veeco Dimension 3100 AFM and apply negative voltages in the range of 16 – 30V to the tip. The AFM is operated in the tapping mode where the damping of the oscillation amplitude is kept constant. This mode is known to give greater stability in the lithography process compared to the contact mode where the repulsive force between the tip and sample is kept constant. The humidity in the environment is controlled by enclosing the sample and tip in a chamber through which a regulated flow of nitrogen passing through DI water is maintained. The chamber's relative humidity is maintained at 35%. This leads to the formation of a thin water meniscus on the tip which acts as the electrolyte for the oxidation reaction. The electric field between the tip and the sample breaks down water into  $H^+$  and  $OH^-$  ions which eventually oxidizes the GaAs surface to form  $Ga_2O_3$  and  $As_2O_3$ . The chemical reaction leading to the oxidation of GaAs is given by [33]:



The height and homogeneity of the oxide lines written are very sensitive to certain parameters.

(i) Sample surface quality : It's imperative that the surface is cleaned very well using the three solvent procedure : Trichloroethylene, Acetone, Isopropyl alcohol. This is followed by a 15 sec dip in a HF:DI (1:10) solution which hydrogenates the

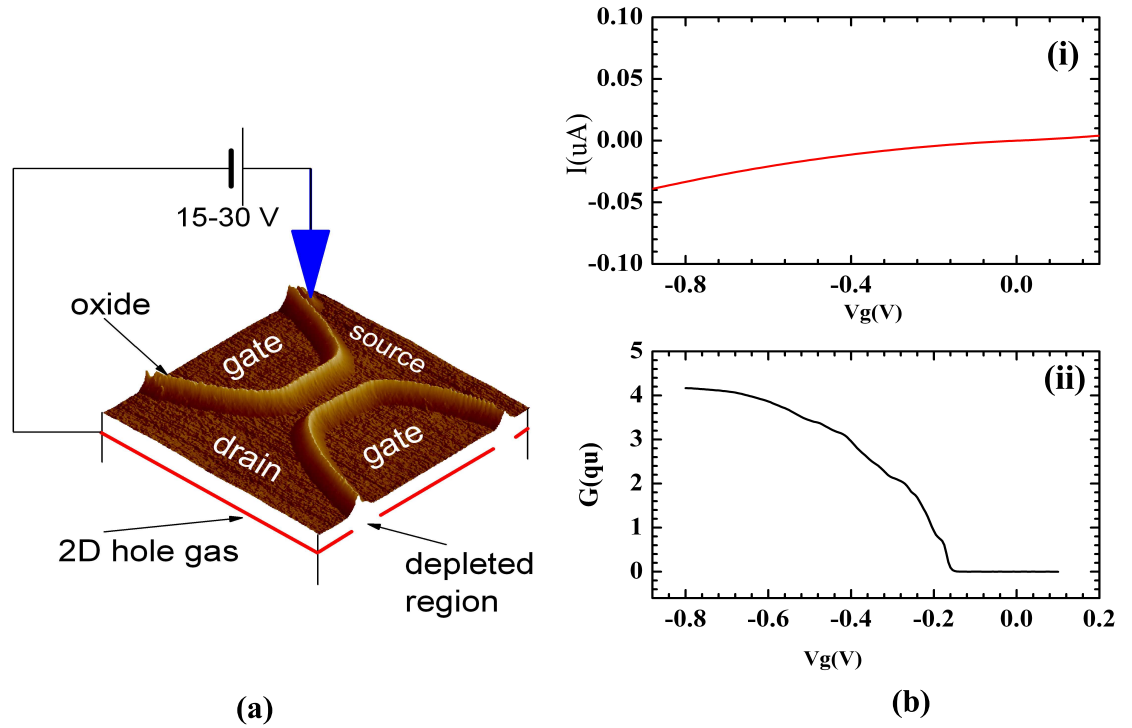


Figure 2.5. (a) Schematic of the setup for the AFM local anodic oxidation procedure. 3D micrograph of the sample indicates the source, drain and gate regions which are separated by the oxide lines. The oxide lines are drawn using a negative bias on the AFM tip (blue arrow). (b)(i) Leakage current across the oxide line for the device at 4K. (b)(ii) Conductance of the quantum point contact as a function of the gate voltage (both gates ramped together) at 4K.

surface. The sample is then flushed with DI water for 2 mins. This last step is crucial to make sure all dangling bonds are substituted with hydrogen which is then removed during the oxidation process.

(ii) Tip quality : Devices in this thesis were made using Mikromasch NSC15 Si tips which are processed in batches. Typical resonant frequency and force constant of the tips are  $\sim 325$  kHz and 40N/m respectively. Characterizing tips prior to writing a device is always desirable since the tip quality can vary even within the same batch. The tip quality can be inferred from the quality of the images. The image from an AFM depends on the shape of the tip. The feature size that can be resolved is dependent on the radius of curvature of the tip. Smaller the radius, smaller the size of features that can be resolved. By imaging a feature on the sample whose size is known, the sharpness of the tip can be inferred. Tips get blunt with use and this step can prove crucial to avoid misinterpreting feature sizes of devices written using LAO. The shape of the tip can also be distorted due to accumulation of dirt from the sample. This could result in spurious feature sizes and shapes. The dirt sometimes gets deposited on the device while scanning. This can be removed by applying large voltages (20-40V) for short durations while scanning regions unimportant to the device or cleaning the tip using isopropyl alcohol. Another important feature of the tip that affects images is the sidewall angle. Tip cannot image sides of features that are steeper than the sidewall of the tip. Knowing this parameter of the tip is important to get the correct width of oxide(etched)lines. A more detailed description of all the tip parameters and their relation to imaging can be found in [34].

(iii) Tip voltage: The width of the lines are known to increase with increasing negative voltages on the tip. It was shown in [35] that biasing the tip with a square modulated ac voltage increases the reproducibility and aspect ratio of the oxide lines. Following that lead we modified our circuit to add AC voltage to the tip, as explained in fig. 2.6. The circuit is designed to modulate the DC bias on the tip with an AC source at a frequency  $\sim 2-3$  kHz. In our experiments we found that using ac voltages helps in initiating the oxidation process at lower voltages ( $\sim 12-15$ V) than with dc

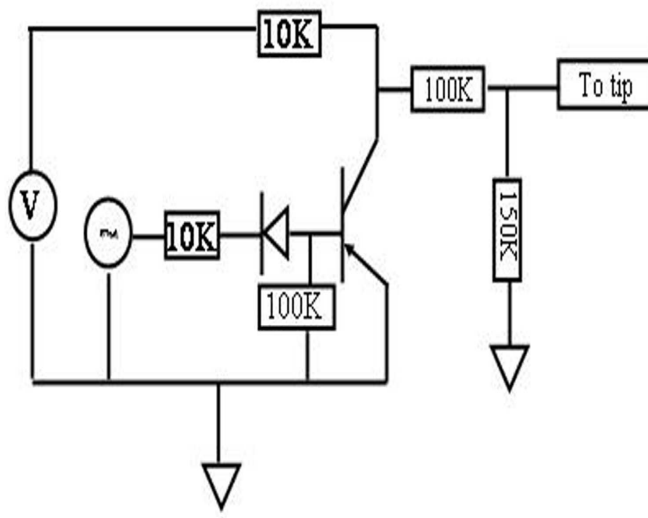


Figure 2.6. Schematic of the circuit to add AC voltage to the tip bias. This circuit adds negative end of the cycle.

voltages.

(iv) Humidity : Maintaining the humidity of the AFM chamber is crucial to make sure the water meniscus formed between the tip and the sample is not too thick. Increased humidity leading to a thicker meniscus results in thicker oxide lines and thermal drifts.

The formation of an oxide layer  $\sim 10\text{nm}$  high on the sample effectively brings the surface states closer to the deeper lying 2DHG by roughly the same distance thereby depleting the 2DHG. For this to be effective it has been experimentally observed that the 2DHG should not be deeper than  $40\text{nm}$  [28]. This imposes some conditions on the kind of heterostructures that can be used to fabricate devices using this method.

Regions of 2DHG separated by oxide lines can be used as in-plane gates for the tuning of many low dimensional devices. Fig. 2.5 shows a quantum point contact fabricated using LAO. A narrow quantum channel is formed ( $0.15\mu\text{m}$  wide) between two oxide lines which separate the 2DHG into source, drain and gate regions as labeled. The oxide lines are insulating at  $4\text{K}$  for voltages in the range :  $-0.5\text{V} \rightarrow +0.5\text{V}$ . The voltage range increases as the temperature is lowered.

## 2.6 Experimental setup

The energy scales we probe in our experiments on quantum point contacts are of the order of  $100\mu\text{eV}$ . In order to observe the various transport phenomena we are interested in, we need temperatures at which the thermal smearing of energy levels (with a Fermi-Dirac distribution),  $3.5k_B T$ , is well below these energy scales. At a temperature of 300mK thermal smearing ( $\sim 88\mu\text{eV}$ ) is barely below the interesting energy scales. While effects like conductance quantization in one dimension are visible at these temperatures, reducing the temperature by another factor of 10 is essential to do accurate energy spectroscopy in 1D systems.

### 2.6.1 Dilution Refrigerator

We use a Kelvinox Oxford dilution refrigerator to obtain the ultra low temperatures needed to study our samples. The principle of operation of a dilution fridge is based on the fact that cooling down a mixture of  $\text{He}^3/\text{He}^4$  below a temperature of 0.8K separates them into two phases: a dilute phase (dilute in  $\text{He}^3$ ) and a concentrated phase, (rich in  $\text{He}^3$ ). Since the enthalpy of  $\text{He}^3$  in the two phases is different, evaporating  $\text{He}^3$  out of the concentrated phase into the dilute phase provides a mechanism for efficient cooling.

A schematic of the dilution refrigerator is shown in Fig. 2.7. The 1K pot is used first to cool the unit down to 1.2K by pumping on it. The first segment of the dilution fridge to cool below 1.2K is the still. It cools the incoming  $\text{He}^3$  before it reaches the mixing chamber. It is important to maintain an optimum volume of the mixture and the percentage of  $\text{He}^3$  in it, such that the phase boundary is formed in the mixing chamber and the liquid surface is in the still. Pumping on the liquid in the still removes  $\text{He}^3$  preferentially, as the partial pressure of  $\text{He}^3$  is 1000 times larger than that of  $\text{He}^4$  at temperatures below 1K. The resultant decrease in the concentration of  $\text{He}^3$  in the dilute phase in the still compared to that in the mixing chamber causes  $\text{He}^3$  to evaporate from the concentrated phase into the dilute phase in the mixing

chamber causing the system to cool further. The difference in pressure causes a flow of  $\text{He}^3$  from the mixing chamber to the still. A small amount of heat is supplied to the still to maintain this flow. The outgoing  $\text{He}^3$  from the mixing chamber is used to cool the incoming mixture via heat exchangers.

The sample is mounted on a thermally annealed copper tail which is in thermal contact with the mixing chamber.

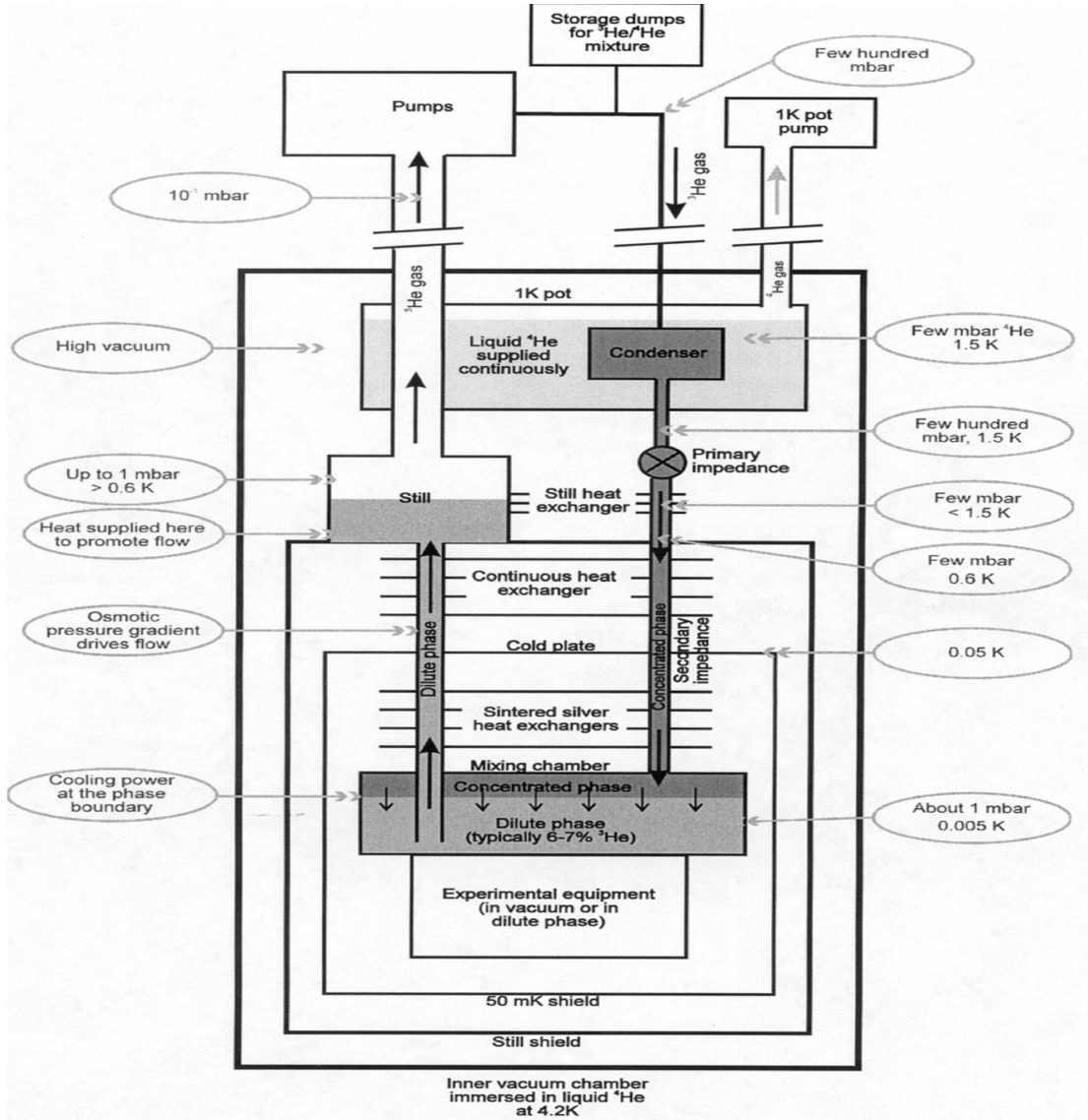


Figure 2.7. Schematic of a Kelvinox 100 Oxford Dilution Refrigerator

### 3. ANISOTROPIC MODIFICATION OF THE EFFECTIVE HOLE $g$ -FACTOR BY ELECTROSTATIC CONFINEMENT<sup>1</sup>

#### 3.1 Introduction: $g$ -factor of two dimensional hole systems

Landé  $g$ -factor is the parameter that determines the linear term in spin-splitting (also known as Zeeman splitting) of energy levels in the presence of a magnetic field. While for bulk systems the Zeeman splitting is independent of the direction of the magnetic field, for quasi-2D systems the reduced symmetry gives rise to different  $g$ -factors for in-plane and out of plane magnetic fields. In general,  $g_{\parallel} < g_{\perp}$  [36].

In two-dimensional GaAs hole gases (2DHG) grown along [001] crystallographic direction, SO locks spins in the growth direction resulting in a vanishing spin response to the in-plane magnetic field (vanishing effective Landé  $g$ -factor  $g^*$ ) [5, 6]. For high-index growth directions, such as [311], in-plane  $g^*$  is not zero and becomes highly anisotropic [7, 8] with  $g_{[233]}^*$  4 times higher than  $g_{[1\bar{1}0]}^*$ . This huge anisotropy is attributed to the highly anisotropic spin-orbit (SO) interactions in these systems. Additional lateral confinement increases  $g^*$  anisotropy [37] and the value depends on the population of 1D subbands [14]. Strong suppression of  $g^*$  for the in-plane magnetic field perpendicular to the channel direction has been attributed to the confinement-induced re-orientation of spins perpendicular to the 1D channel [37].

In this study, we demonstrate that the anisotropy of spin splitting is primarily due

---

<sup>1</sup>S. P. Koduvayur, L. P. Rokhinson, D. C. Tsui, L. N. Pfeiffer, and K. W. West, “Anisotropic modification of the effective hole  $g$ -factor by electrostatic confinement”, Physical Review Letters 100, 126401 (2008);arXiv:0802.4271

to the crystalline anisotropy of SO interactions and not the lateral confinement. We investigate quantum point contacts with confinement in both  $[1\bar{1}0]$  and  $[\bar{2}33]$  directions and find that anisotropy of spin splitting depends on the field direction rather than on the direction of the lateral confinement. There is a strong dependence of  $g^*$  on the number of filled 1D subbands  $N$  for one crystallographic direction ( $B\parallel[\bar{2}33]$ ), while  $g^*$  is almost  $N$ -independent for the orthogonal field direction ( $B\parallel[1\bar{1}0]$ ). We also report qualitative differences in the appearances of the conductance plateaus for the two orthogonal confinement directions. For the channels confined in  $[\bar{2}33]$  direction the conductance of spin-split plateaus is  $(N + 1/2)e^2/h$ , in accordance with Landauer formula. For the orthogonal directions non-quantized plateaus appear. These plateaus have some resemblance to the so-called “0.7 structure” [38] and its various “analogs” [39] and their conductance values change with magnetic field. The major difference between the two orientations of 1D channels in our experiments is the strength of SO, which may provide some clue to the origin of these yet-to-be-understood anomalies.

### 3.2 Sample details and experimental observations

The QPCs are fabricated from high mobility ( $\mu \sim 0.4 \times 10^6$  Vs/cm<sup>2</sup>) low density ( $p \sim 1.4 \times 10^{11}$  cm<sup>-2</sup>) 2D hole gas grown on [311]A GaAs. We use AFM local anodic oxidation [31, 32] to fabricate the QPCs as described in the Introduction chapter of this thesis. An AFM image of the QPC device measured is shown in Fig. 3.1(c). QPCs #a and #c are confined along  $[\bar{2}33]$  and QPC #b is confined along the perpendicular  $[1\bar{1}0]$  direction. White lines are oxide which separates 2DHG into source (S), drain (D) and gate (G) regions, the 2DHG is depleted underneath the oxide. The side gates are used to control electrostatically the width of the 1D channel. AFM lithography aids in precise control of QPC dimensions with corresponding pinch-off voltage control within a few mV, which allows us to compare orthogonal QPCs with similar confining potential. At  $T = 4$  K, QPCs show regular smooth FET characteristics as a function

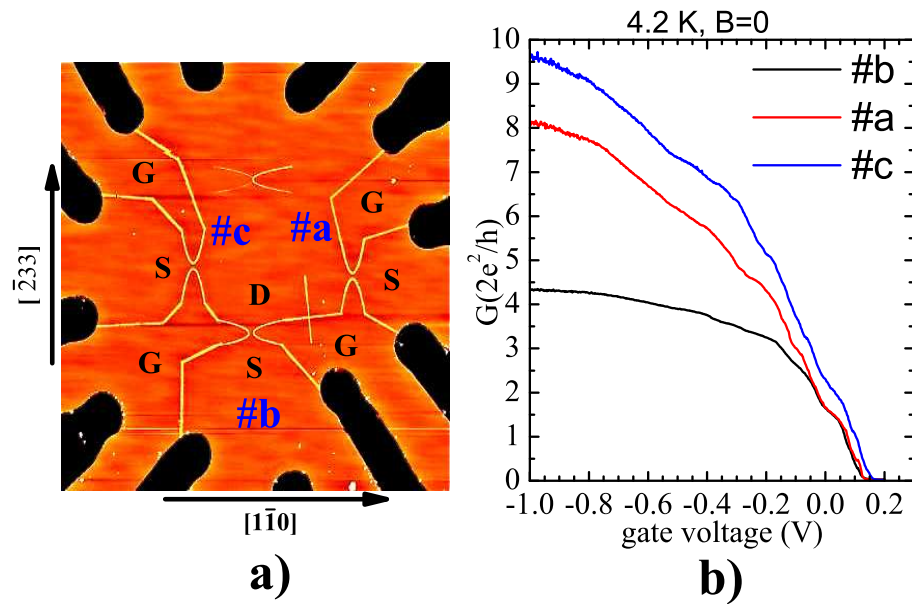


Figure 3.1. (a) AFM micrograph of 3 QPCs fabricated on the same sample. #a and #c are confined along  $[\bar{2}33]$  and #b is confined along  $[1\bar{1}0]$ . (b) Conductance of the QPCs shown in (a) as a function of gate voltage at 4K and  $B=0$ .

of gate voltage (Fig. 3.1(b)). For orthogonal QPCs with similar pinch-off voltages, resistances differ by a factor of two, reflecting the underlying anisotropy of the 2DHG. Conductivity of 2DHG on  $[311]$  GaAs is anisotropic due to a combination of effective mass anisotropy and difference in surface morphology, with  $[\bar{2}33]$  being high-mobility and  $[1\bar{1}0]$  low-mobility directions [27].

Conductance traces at low temperatures were studied for  $\sim 10$  samples. A typical device (with the best quantized conductance steps among those measured) is analyzed in the following section. Conductance at low temperatures along the two orthogonal directions is shown in Fig. 3.2. The blue curves are measured for  $B = 0$ . Four-terminal resistance is corrected for the gate-independent series resistance of the adjacent 2D gas,  $R_0 = 300 - 600 \Omega$  in all the samples measured.  $R_0$  was also corrected for its  $B$ -dependence which was measured separately for both crystallographic directions (a

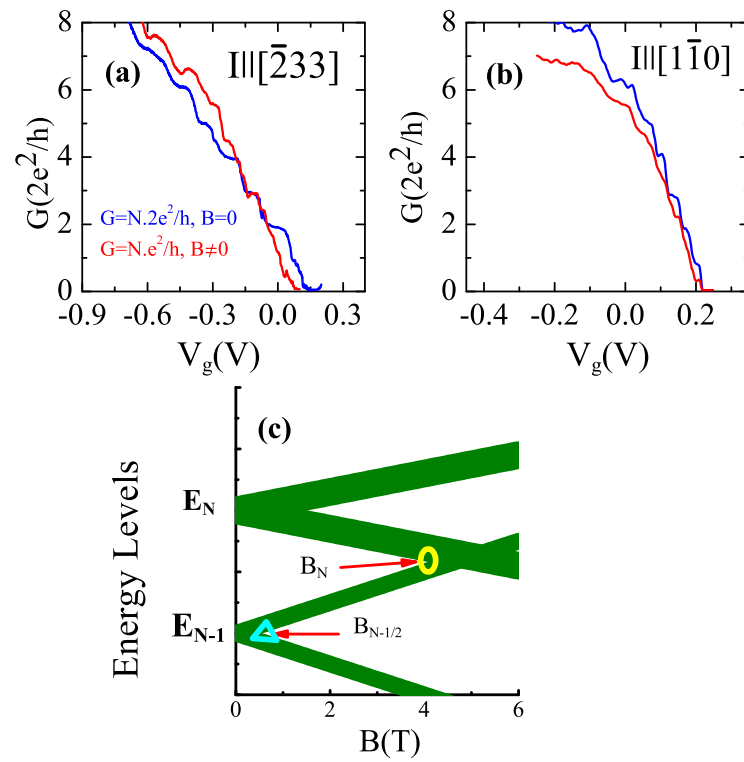


Figure 3.2. Conductance of the QPCs at  $T=30\text{mK}$  for  $B = 0T$  (blue curve) and  $B = 12T$  (red curve) confined along  $[1\bar{1}0]$  (a) and along  $[2\bar{3}3]$  (b). (c) Schematic of Zeeman splitting of energy levels showing fields at which spin splitting occurs and two levels cross.

20% increase at 12T). At low temperatures conductance is quantized [9, 10, 13] in units of  $G = Ng_0$ , where  $g_0 = 2e^2/h$  and  $N$  is the number of 1D channels below the Fermi energy, which reflects the exact cancellation of carriers velocity and the density of states in 1D conductors. The factor 2 reflects spin degeneracy of energy levels at  $B = 0$ . Plateaus appear when electrochemical potentials of source and drain lay in the gap between neighboring 1D subbands  $E^N$  and  $E^{N+1}$ . In various samples we resolve up to 8 plateaus at temperatures  $T < 100$  mK. The samples were rotated either *in situ* (Fig. 3.4) or after thermo-cycling to room temperature (Fig. 3.3). Mesoscopic changes during thermo-cycling are reflected in a small difference between the  $B = 0$  curves, yet they do not change level broadening and onset of spin splitting significantly.

### 3.3 Effect of in-plane magnetic field

In general the 2D energy spectrum for holes contains linear, cubic and higher-order terms in  $B$  [36]. At low fields linear term dominates and we will approximate spin splitting by the Zeeman term with an effective  $g$ -factor,  $E_Z = 2g_{[ijk],N}^* \mu_B B$ , where  $\mu_B$  is the Bohr magneton and  $g_{[ijk],N}^*$  depends on field orientation  $B \parallel [ijk]$ , energy level number  $N$  and confinement direction. Half-integer plateaus appear at critical fields  $B^{N+1/2}$ , when spin splitting of the  $N$ -th level becomes equal to the disorder broadening of the level, as shown schematically in Fig. 3.2(c). At sufficiently higher fields, conductance is quantized in units of  $e^2/h$ , where the  $B = 0$  integer plateaus disappear (Fig. 3.2(a)&(b) red curves).

Effect of in-plane magnetic field on conductance is shown in Figs. 3.3 and 3.4 for the two orthogonal field direction. The curves are offset proportional to the magnetic field with 0.25T increments. For the sample studied in Figs. 3.3 (a,b) the 1D channel is confined in  $[\bar{2}33]$  direction ( $I \parallel [1\bar{1}0]$ ), while those in Figs. 3.3 (c,d) and 3.4 (a,b) are confined in  $[1\bar{1}0]$  direction ( $I \parallel [\bar{2}33]$ ).

There are both quantitative and qualitative differences in the field response of orthogonally oriented 1D channels. We will start the analysis with quantitative com-

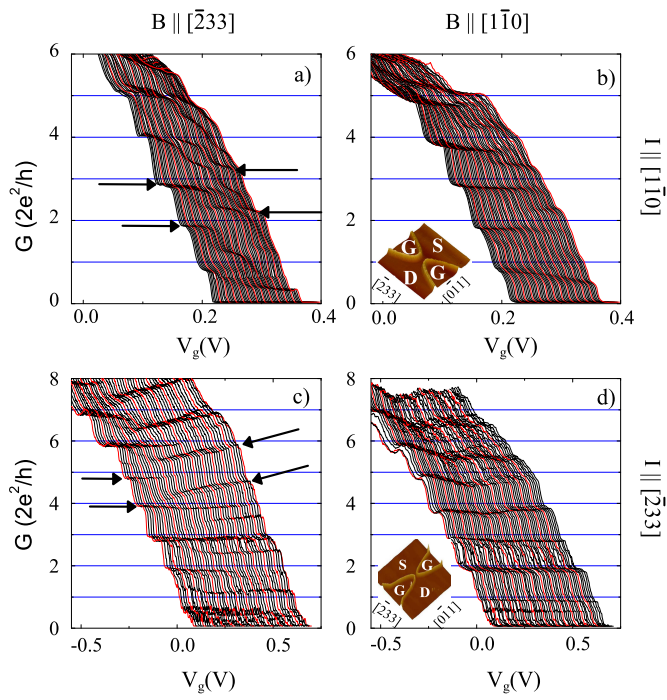


Figure 3.3. Conductance of a QPC as a function of gate voltage. The curves are offset proportional to  $B$  with 0.25 T interval. Leftmost curve corresponds to  $B = 0$ . (a,b) are for the channel along  $[1\bar{1}0]$  and (c,d) for the channel along  $[\bar{2}33]$ . The arrows highlight a few plateaus discussed in the text, the slope of the arrows highlighting the slope of the corresponding plateau. Insets:  $2\mu\text{m} \times 2\mu\text{m}$  AFM micrographs of devices.

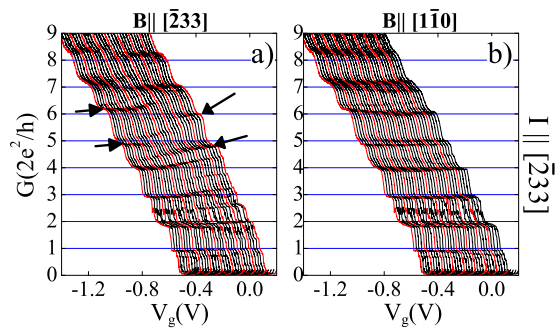


Figure 3.4. Conductance of another QPC with the channel oriented along  $[\bar{2}33]$ . The curves are offset proportional to  $B$  with  $0.25 T$  interval. Leftmost curve corresponds to  $B = 0$ . The arrows highlight plateaus discussed in the text.

parison of spin splitting of energy levels for different orientations of magnetic field and channel directions. While level broadening is different for different energy levels we expect it to be independent of the direction of the magnetic field and the ratio of  $g^*$ 's for the two orthogonal crystallographic directions can be obtained from the appearance of half-integer plateaus,  $B_{[1\bar{1}0]}^{N-1/2}/B_{[233]}^{N-1/2} = g_{[233],N}^*/g_{[1\bar{1}0],N}^*$ . The integer plateaus disappear at the fields  $B^N$  when two neighboring levels with opposite spin intersect, and the average  $\langle g_{[ijk],N}^* \rangle = (g_{[ijk],N}^* + g_{[ijk],N+1}^*)/2$  can be found from  $\Delta E_N = \Delta E_z = \langle g_{[ijk],N}^* \rangle \mu_B B_{[ijk]}^N$ , where  $\Delta E_N$  is the zero-field energy spacing of 1D subbands excluding level broadening.

Splitting and crossing of energy levels are best visualized in transconductance plots. In Fig. 3.5(a,b) a grayscale of  $dG/dV_g$  for the data in Fig. 3.3(a,b) is plotted. The white regions correspond to the plateaus, the dark regions correspond to the energy level being aligned with the Fermi energy in the leads and reflect level broadening, which is found to be roughly half of the level spacing in our samples. At low fields the width of the plateaus decreases almost linearly with field, which justifies the use of linear approximation. There is clear deviation from linear dependence at higher fields. The critical fields where levels cross ( $B^N$ ) and split ( $B^{N-1/2}$ ) are indicated by triangles and circles.

### 3.4 Non-linear transport spectroscopy

Level spacing is determined from non-linear transport spectroscopy. When a DC bias is applied to the source-drain, new plateaus appear that are quantized at half-integer values. These half-integer plateaus are understood to appear when the number of conducting subbands in the forward and backward direction of transport differ by 1 [40–42]. A gray scale plot of transconductance is shown in Fig. 3.5(c). The plot is in logarithmic scale with white regions representing the plateaus. By determining the maximum current  $I_{max}$  for the  $N^{th}$  plateau at which the transconductance is still zero we obtain the 1D subband spacings between levels  $N$  and  $N + 1$  excluding level

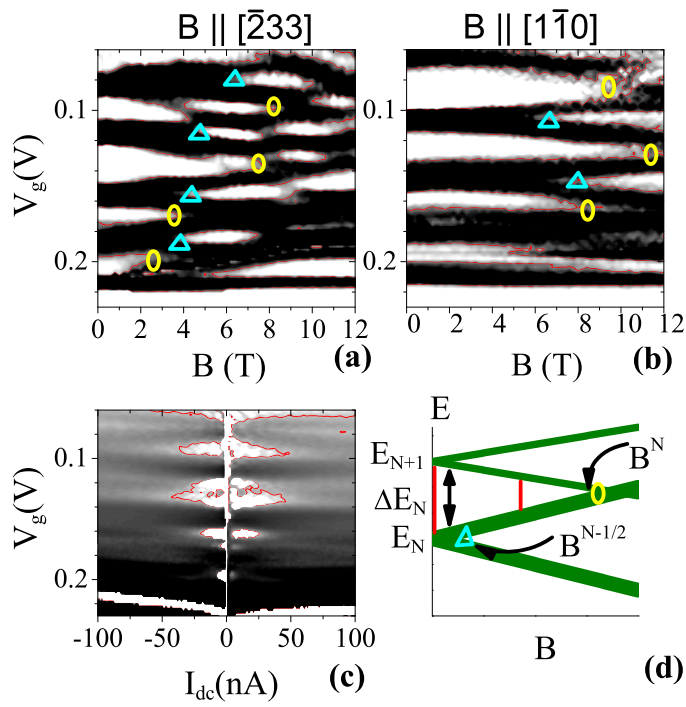


Figure 3.5. (a,b) Derivative of curves in Fig 3.3, white regions correspond to the conductance plateaus. (c) Differential transresistance plotted in a logarithmic scale (from  $0.01 \text{ k}\Omega$  (white) to  $0.2 \text{ k}\Omega$  (black)) for the same sample at  $B = 0$ . (d) Schematic of Zeeman splitting of energy levels.

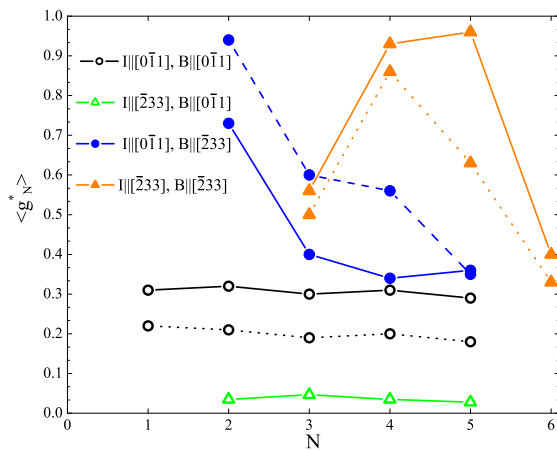


Figure 3.6. (a) Average  $g_N^*$  between adjacent levels  $N$  and  $N + 1$  is plotted for different orientations of channel and magnetic field. Open and filled symbols are for magnetic field parallel to  $[1\bar{1}0]$  and  $[\bar{2}33]$ , respectively. Circles and triangles are for channels along  $[1\bar{1}0]$  and  $[\bar{2}33]$ , respectively. The blue dashed curve is the actual  $g_N^*$  for  $I||[1\bar{1}0], B||[\bar{2}33]$ . The orange and black dotted curves are corrected for the diamagnetic shift.

Table 3.1  
Summary of experimental values used to extract  $g^*$  for different energy levels for channel along  $[1\bar{1}0]$ .

Channel along  $[1\bar{1}0]$

$N$	$R$ (k $\Omega$ )	$I_{max}$ (nA)	$\Delta E_N$ ( $\mu$ eV)	$B_{[233]}^N$ (T)	$\langle g_{[233],N}^* \rangle$	$B_{[0\bar{1}1]}^N$ (T)	$\langle g_{[0\bar{1}1],N}^* \rangle$	$\frac{B_{[0\bar{1}1]}^{N-1/2}}{B_{[233]}^{N-1/2}} = \frac{g_{[233]}^*}{g_{[0\bar{1}1]}^*}$	$g_{[233]}^*$
1	12.9	6	80			4.5	0.31		
2	6.45	23	150	3.6	0.73	8	0.32	3	0.94
3	4.3	40	170	7.5	0.4	10	0.30	2	0.6
4	3.225	50	160	8	0.34	9	0.31	1.8	0.56
5	2.58	60	150	7.3	0.36	9	0.29	1.2	0.35

Table 3.2  
Summary of experimental values used to extract  $\langle g^* \rangle$  for different energy levels for channel along  $[\bar{2}33]$

Channel along  $[\bar{2}33]$

$N$	$R$ (k $\Omega$ )	$I_{max}^{B=0}$ (nA)	$\Delta E_N^{B=0}$ ( $\mu$ eV)	$I_{max,[0\bar{1}1]}^{ST}$ (nA)	$\Delta E_{N,[0\bar{1}1]}^{ST}$ ( $\mu$ eV)	$\langle g_{[0\bar{1}1],N}^* \rangle$	$B_{[233]}^N$ (T)	$\langle g_{[233],N}^* \rangle$
2	6.45	25	161.25	22.5	145.13	0.035		
3	4.3	27.5	118.25	22.5	96.75	0.046	3	0.56
4	3.225	50	161.25	45	145.13	0.0347	3	0.93
5	2.58	42.5	109.65	37.5	96.75	0.028	6	0.96
6	2.16	35	75.6				3.25	0.4

broadening as  $\Delta E_N = eRI_{max}$ , where  $R = h/2Ne^2$  is the resistance on the plateaus.

The experimental data for the channel along  $[1\bar{1}0]$  is summarized in Table 3.1. We obtain the energy level spacing  $\Delta E_N$  for the first five energy levels using the above explained method. From the critical fields  $B^N$  we obtain the average  $\langle g_{[ijk],N}^* \rangle$  for the neighboring energy levels. The ratio of the  $g^*$ s is 3 for  $N = 1$  and approaches the

2D value of 1.2 for large  $N$ . The values  $\langle g_{[1\bar{1}0]}^* \rangle$  do not depend on  $N$  and we use  $g_{[1\bar{1}0]}^* = 0.3$  to obtain the values for  $g_{[\bar{2}33]}^*$  from the ratios  $g_{[\bar{2}33],N}^*/g_{[1\bar{1}0],N}^*$ . In Table 3.2 we present similar data for QPCs with the channel along  $[\bar{2}33]$  direction. For these samples no half-split plateaus are observed for  $B \parallel [1\bar{1}0]$  and  $B^{N-1/2}$  is unattainable. We still can extract the average  $\langle g^* \rangle$  values by measuring the change in the energy level spacing  $\Delta E_N(0) - \Delta E_N(B) = \langle g^* \rangle \mu_B B$ , as shown by bars in the schematic in Fig. 3.5(d). For  $B \parallel [\bar{2}33]$  the introduction of  $g^*$  has questionable meaning due to anomalous behavior of half-integer plateaus and ill-defined  $B^{N-1/2}$ . We estimate  $g^*$  from the measured  $B^N$ .

Fig. 3.6 summarizes our results for the  $g^*$  for different confinement directions. For  $B \parallel [\bar{2}33]$  spin splitting of energy levels strongly depends on the level number  $N$  for both confinement directions. For the field  $B \parallel [1\bar{1}0]$ ,  $g^*$  is smaller and is almost independent of  $N$ . We conclude that  $g$ -factor anisotropy is primarily determined by the crystalline anisotropy of spin-orbit interactions. Lateral confinement enhances the anisotropy.

### 3.5 Effect of diamagnetic shift on $g$ -factor anisotropy

So far we ignored diamagnetic shift of energy levels, which is the shift of 2D subbands as a function of applied magnetic field. The ratios  $g_{[\bar{2}33],N}^*/g_{[1\bar{1}0],N}^*$  are not affected by this shift because they characterize energy difference between spin states of the same orbital level. Likewise, the extracted  $\langle g^* \rangle$  will not be affected by field confinement in the growth direction because the first 8-10 1D levels belong to the same lowest 2D subband. The only value to be affected by diamagnetic shift will be  $\langle g^* \rangle$  for  $B \parallel I$ . To estimate the correction we approximate both vertical and lateral confinement by parabolic potentials  $\hbar\omega_z = 2.4$  meV,  $\hbar\omega_y = 0.3$  meV. The corrected  $\langle g_c^* \rangle = \langle g^* \rangle (1 + \frac{\omega_1(B^N) - \omega_1(0)}{\omega_1(0)})$ , where  $\hbar\omega_1 = \frac{\hbar}{2} \sqrt{(\omega_c^2 + \omega_y^2 + \omega_z^2) - \sqrt{(\omega_c^2 + \omega_y^2 + \omega_z^2)^2 - \omega_y^2 \omega_z^2}}$  is the field dependent energy spacing for spinless particles [43],  $\omega_c = eB/m_c$  is the cyclotron frequency, and  $m_c = \sqrt{m_h m_l} = 0.28m_e$  is the cyclotron mass. For  $I \parallel [\bar{2}33]$

the critical fields  $B_{[\bar{2}33]}^N \sim 3$  T are small and correction to  $\langle g^* \rangle$  due to the diamagnetic shift is  $< 5\%$ . For the channel along  $[\bar{1}\bar{1}0]$   $B_{[\bar{1}\bar{1}0]}^N \sim 8 - 10$  T and correction is  $\sim 30\%$  which is not negligible. We plot the corrected values in Fig. 3.6.

### 3.6 Unusual qualitative behavior of “half-integer” plateaus

Now we will highlight a few qualitative differences in the appearance of “half-integer” plateaus for the channels along  $[\bar{1}\bar{1}0]$  and  $[\bar{2}33]$  directions. Conductance of spin-split plateaus for channels along  $[\bar{1}\bar{1}0]$  are quantized at  $G = (N + 1/2)g_0$ , in full agreement with the theory. In point contacts with confinement in the orthogonal direction, conductance of spin-split plateaus is not quantized and is field dependent. At low fields ( $B < 4$  T) their evolution resembles “0.7 structure” and various anomalous plateaus reported in electron samples. At higher fields the conductance of these plateaus increases with magnetic field, at the same time the integer plateaus remain quantized at  $Ng_0$ . We emphasize the motion of spin-split plateaus with the slope of arrows in Figs. 3.3 and 3.4. For example, in Fig. 3.3(c) a plateau at  $4.3g_0$  appears at  $B \sim 3$  T and its value gradually increases to  $\sim 4.8g_0$  by 12 T. The next non-integer plateau appears at  $B \sim 3$  T and increases to  $\sim 6g_0$  by  $B = 12$  T. At the same time, the neighboring integer plateaus remain quantized at  $G = 4g_0, 5g_0$  and  $6g_0$ . This feature has been observed consistently in all the samples we measured, as is evident from Fig. 3.4, where similar data is presented for a different sample: a plateau at  $5.2g_0$  appears at  $B \sim 3.3$  T and increases to  $\sim 6g_0$  by 8 T. The orthogonal 1D channels are fabricated from the same 2D hole gas and have similar confinement potentials. The only difference is due to the anisotropy of spin-orbit interactions. Thus, we conclude that spin-orbit interactions are responsible for the anomalous behavior.

### 3.7 Conclusion

To summarize the results, we investigate effects of lateral confinement on spin splitting of energy levels in 2D hole gases in  $[311]\text{GaAs}$ . We found that lateral con-

finement enhances anisotropy of spin splitting relative to the 2D gas for both confining directions. Unexpectedly, the effective  $g$ -factor does not depend on the energy level number  $N$  for  $B\|[\bar{1}\bar{1}0]$  while it has strong  $N$ -dependence for the orthogonal orientation,  $B\|[\bar{2}33]$ . We also observe qualitative differences in the appearance of spin-split plateaus for the two orthogonal directions of lateral confinement, which we can attribute to the difference in spin-orbit interaction.

## 4. EFFECT OF STRAIN ON NEMATIC PHASES IN TWO DIMENSIONAL HOLES<sup>1</sup>

### 4.1 Nematic phases in Quantum Hall systems

Interplay between kinetic energy and electron-electron interactions in two-dimensional electron gases in magnetic fields leads to a rich variety of possible ground states, ranging from incompressible Laughlin liquids, the Wigner crystal, charge density waves (CDW) to exotic non-Abelian anyonic states. The possibility of the formation of a CDW state had been suggested [17] even before the discovery of the quantum Hall effect, and later it was predicted that a CDW should be the ground state for partially occupied high Landau levels [18, 19]. Experimentally, anisotropic magnetoresistance (AMR) has been observed in 2D electron [21, 22] and hole [23, 24] gases. The majority of experiments have been conducted on samples grown on (001) GaAs. Unexpectedly, the CDW was found to be consistently oriented along [110] crystallographic direction in these samples, a surprising fact considering the isotropic nature of the wave functions on the high symmetry (001) surface.

Search for the physical origin of the broken symmetry and the observed preferential orientation of stripe phases has been actively pursued experimentally and theoretically over the past decade. Reduced symmetry of the interface was suggested [44] as a factor which introduces an anisotropy of the effective mass [45] or of the cyclotron motion [46]. However, single-particle effects associated with these anisotropies seem unlikely to be responsible for the large magnitude and strong temperature dependence

---

<sup>1</sup>Sunanda P. Koduvayur, Yuli Lyanda-Geller, Sergei Khlebnikov, Gabor Csathy, Michael J. Manfra, Loren N. Pfeiffer, Kenneth W. West, “Effect of strain on stripe phases in the Quantum Hall regime” arXiv:1005.3327v1

of the resistance [47]. Later work showed [48] that the precise symmetry of the 2D gas confining potential is also unimportant, and micron-scale surface roughness does not correlate with the stripe orientation. There have been theoretical suggestions [49–51] that anisotropic correction to electron-electron interactions arising from elastic and piezoelectric effects can be responsible for the resistance anisotropy. While the free energy of the CDW is minimized in the vicinity of  $[110]$  and  $[1\bar{1}0]$  directions, those theories cannot explain why these directions are inequivalent. Progress has been made in understanding the effect of the in-plane magnetic field, which has been shown to influence orientation of stripes [52, 53], the effect being explained by the field-induced anisotropy of the exchange potential [54, 55]. However, naturally existing preference for  $[110]$  orientation of the CDW in purely perpendicular field, the same for electron and hole samples, remained unresolved.

In this work we show both experimentally and theoretically that strain breaks the symmetry of electron-electron interactions in magnetic field and results in a preferred orientation of the CDW. We show experimentally that externally applied shear strain can enhance or reduce anisotropy of the resistance and switch low and high resistance axes. Our theory shows that spin-orbit interaction induced anisotropy of spectrum in the absence of strain results in  $[110]$  or  $[1\bar{1}0]$  being the preferential directions of CDW, which are equivalent; in plane shear strain breaks the symmetry between these two directions, and depending on its sign, the Hartree-Fock energy is minimized when the CDW is oriented along one of these directions. We suggest that shear strains due to internal electric fields in the growth direction caused by mid gap Fermi level pinning at the sample surface are responsible for the observed preferred orientation of the CDW in externally unstrained electron and hole samples. Finally, we find that strain induces a stripe phase at a filling factor  $\nu = 5/2$ , with a CDW winning over other QH states.

## 4.2 Sample and Experimental setup details

Samples were fabricated in the van der Pauw geometry, with In/Zn contacts, from carbon doped GaAs quantum well heterostructure grown on (001) GaAs [24, 30]. From the low field Shubnikov de-Haas oscillations, the hole density is  $2.25 \times 10^{11} \text{ cm}^{-2}$ , and the mobility  $0.8 \times 10^6 \text{ cm}^2/\text{Vs}$  is determined at the base temperature 10mK. Some samples were thinned to  $150 \mu\text{m}$  and glued on a multilayer PZT (lead zirconate titanate) ceramic actuator with vacuum grease, which solidifies below  $80\text{K}$  transmitting the strain to the sample as efficiently as the epoxy used in previous studies [56]. The samples'  $[110]$  or  $[1\bar{1}0]$  crystallographic axis is aligned with the polarization axis of the PZT. Application of voltage  $V_p$  to the actuator induces in-plane shear strain in the sample  $\varepsilon_p/V_p = 2.8 \times 10^{-7} \text{ V}^{-1}$  and small uniform bi-axial strain. We characterize the PZT stack at 300 mK by attaching strain gauges along the polarization direction of the PZT and perpendicular to it [56]. The total shear strain  $\varepsilon = \varepsilon_{th} + \varepsilon_p$  also includes a residual strain  $\varepsilon_{th}$  due to anisotropic thermal coefficient of the actuator, which depends on the  $V_p$  during cooldown. To insure that voltage on the actuator does not induce charge modulation in the attached sample we insert a thin metal foil between the sample and the PZT. The foil was also used as a back gate to adjust 2D gas density which has a weak dependence on strain due to difference in piezoelectric coefficients of GaAs and AlGaAs [57] (density changes by 8% for the maximum voltage span on the PZT). Fig. 4.1 shows the change in density as a function of PZT voltage and the corresponding back-gate voltage needed to counter the density change. Simultaneously with the strained sample we also cool an unstrained sample(not attached to the PZT), fabricated from the same wafer as the strained sample and adjacent to it. We cool the samples in a dilution refrigerator with a base temperature of 10mK and use excitation currents of 5nA to measure the resistances.

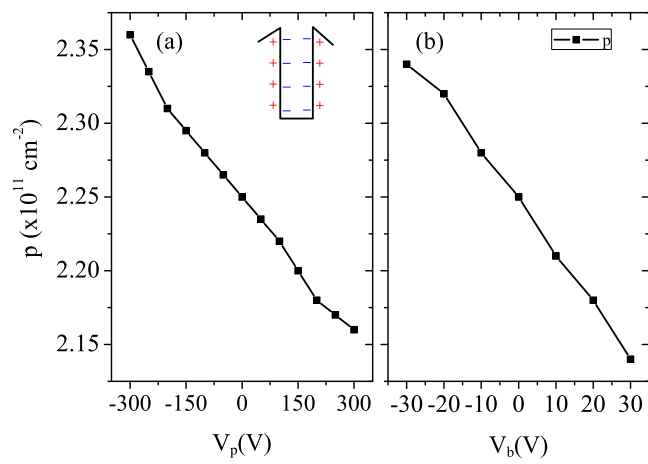


Figure 4.1. (a) Density as a function of PZT voltage. There is an 8% change for the full PZT scan at base temperature. (b) Density as a function of back gate voltage.

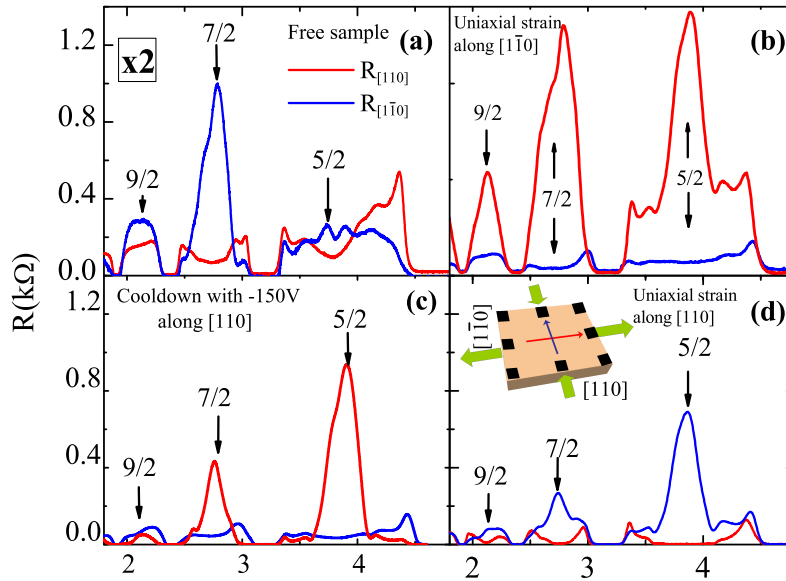


Figure 4.2. Magnetoresistance is plotted as a function of  $\mathbf{B}$  for the current aligned with  $[110]$  (red) and  $[1\bar{1}0]$  (blue) directions in strained and unstrained samples. In (a) no external strain is applied, (b) thermally-induced tensile strain is along  $[1\bar{1}0]$ , and (d) along  $[110]$ , with  $\varepsilon_p = 0$ . (c) The sample is cooled down with  $V_p = -150V$  with  $[110]$  along the poling axis of the PZT. Inset shows sample schematic, red and blue arrows show current, and green arrows show strain.

### 4.3 Effect of external uniaxial strain on nematic phases

Fig. 4.2 shows the major effects of strain on the magnetotransport along  $[110](xx)$  and  $[1\bar{1}0](yy)$  for our samples. Magnetoresistance for externally unstrained (free sample) is shown in Fig. 4.2a. The resistance along  $[1\bar{1}0]$  is scaled to have the same magnitude as the resistance along  $[110]$  at low fields. States at  $\nu = 7/2$  and  $11/2$  are highly anisotropic with low resistance direction along  $[110]$ , while states at  $\nu = 5/2$ ,  $9/2$  and  $13/2$  are almost isotropic, consistent with the previous study [24]. In Fig. 4.2 b,d similar traces are shown for large  $\varepsilon = \varepsilon_{th} \gtrsim +10^{-4}$  and  $\varepsilon = \varepsilon_{th} \lesssim -10^{-4}$  ( $\varepsilon_p = 0$ ). For  $\varepsilon_{th} < 0$ , Fig. 4.2b the anisotropy is enhanced compared to the unstrained sample, with states at  $\nu = 5/2, 9/2$  and  $13/2$  becoming anisotropic and resistance for  $I_{\parallel}[1\bar{1}0]$  approaching zero for half-filled Landau levels. For  $\varepsilon_{th} > 0$ , Fig. 4.2d, the low and high resistance axes are switched. Here strain also leads to strong anisotropy at  $\nu = 5/2$  with low resistance axis along  $[110]$  direction.

Residual strains  $\varepsilon_{th}$  in Fig. 4.2b,d are larger than the *in situ* adjustable strain  $\varepsilon_p$ . The large thermal strains can be offset by cooling down the PZT with some voltage. In Fig. 4.2c we show anisotropic magnetoresistance (AMR) for a sample cooled with  $V_p = -150$  V, aiming for  $\varepsilon_{th} \sim 0$ . While the traces are not same as in a free sample, the anisotropy is definitely reduced compared to Fig. 4.2b, as seen by the reduced resistance of  $R_{[110]}$  at  $\nu = 5/2, 7/2$  and the isotropic  $\nu = 9/2$  state. Analysis of AMR for various filling fractions as a function of  $\varepsilon_p$  is done for this particular cooldown.

Magnetoresistance as a function of  $\varepsilon_p$  is plotted near  $\nu = 5/2$  and  $7/2$  in Fig. 4.3. At  $V_p < 0$  magnetoresistance is highly anisotropic. For high resistance direction, resistance  $R_{I_{\parallel}[110]}$  strongly depends on  $\varepsilon_p$  and decreases by a factor of 50 (4.4) at  $\nu = 5/2$  ( $7/2$ ) as  $V_p$  is varied from -300 V to 300 V.  $R_{I_{\parallel}[1\bar{1}0]}$  increases only 1.7 (1.3) times. At  $V_p > 100$  V, the resistance at  $\nu = 5/2$  is isotropic, with no maxima for either current direction, as in unstrained sample. Thus, in the range of small strains, the CDW is not a ground state at  $\nu = 5/2$ , consistent with observations in unstrained samples. From the data we conclude that  $\varepsilon < 0$  within the adjustable range of  $V_p$ ,

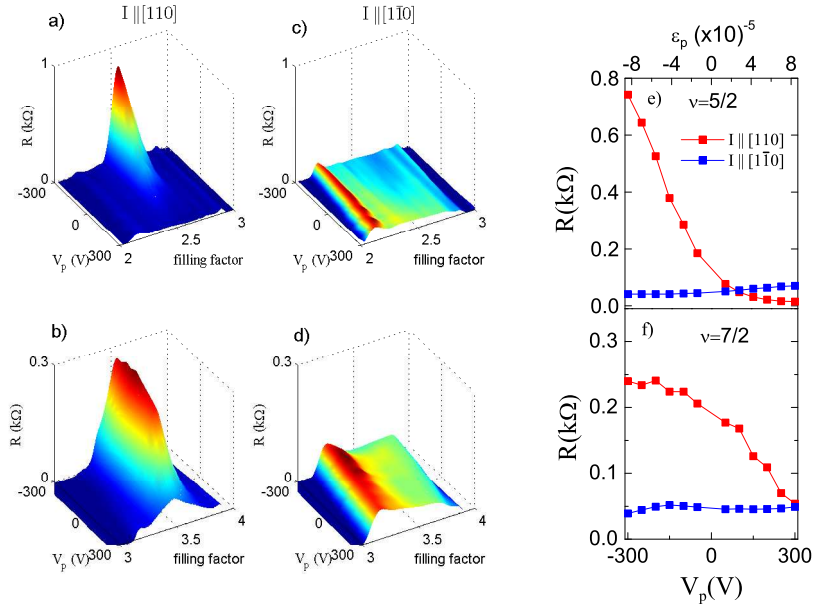


Figure 4.3. Strain dependence of the anisotropic magnetoresistance. (a-d) Magnetoresistance in the vicinity of  $\nu = 7/2$  and  $5/2$  for  $I_{||}[110]$  and  $I_{||}[\bar{1}\bar{1}0]$  as a function of voltage on the piezoelectric actuator  $V_p$ . In (e-f) magnetoresistance at  $\nu = 7/2$  and  $5/2$  is extracted. On the top axis,  $V_p$  is converted to the piezo-induced shear strain in the heterostructure; actual strain includes thermally-induced offset.

because  $R_{I_{||}[110]} > R_{I_{||}[\bar{1}\bar{1}0]}$  at  $\nu = 7/2$ . Continuous evolution of  $R_{I_{||}[110]}$  and  $R_{I_{||}[\bar{1}\bar{1}0]}$  is consistent with continuous change reported with in-plane magnetic field [53].

#### 4.4 Strain-induced anisotropic Hartree-Fock energy for holes

Having presented experimental results of strain on the resistance in the QH regime, I now present the Hartree-Fock theory of CDW developed by Prof. Yuli Lyanda-Geller. The model was obtained by extending earlier theoretical work [18, 19, 58] to anisotropic 2D systems. The Hamiltonian of holes in a strained 3D system is

$$\mathcal{H} = -(\gamma_1 + \frac{5}{2}\gamma_2)k^2 + \gamma_2 \sum_i J_i^2 k_i^2 + \gamma_3 \sum_{i,j \neq i} [J_i J_j] k_i k_j + -(a + \frac{5}{4}b)tr\varepsilon + b \sum_i J_i^2 \varepsilon_{ii} + \frac{d}{\sqrt{3}} \sum_{i,j \neq i} [J_i J_j] \varepsilon_{ij}, \quad (4.1)$$

where  $[J_i J_j] = (J_i J_j + J_j J_i)/2$ ,  $i, j, k$  denote principal axis of the crystal  $\hat{x}_1 \parallel [001]$ ,  $\hat{y}_1 \parallel [010]$  and  $\hat{z}_1 \parallel [001]$ ,  $\mathbf{k}$  is the wavevector of holes, and  $\mathbf{J}$  is the angular momentum  $3/2$  operator describing the top bulk valence band.  $\gamma_1, \gamma_2, \gamma_3$ , and  $a, b, d$  are dimensionless (negative) constants defining the hole spectra [59, 60]. For quantum well confined along (001) 2D spectra for unstrained holes was discussed by Nedoresov [61]. In this work, the effect of transverse strain is considered. It is assumed that the spatial quantization defines the largest energy scale, while strain introduces corrections to size-quantized spectrum. Applying the approximation of infinite rectangular quantum well, the quadratic in  $k_i$  energy spectrum for the highest double degenerate valence hole state in the presence of external or internal strain is

$$E = (2\gamma_2 - \gamma_1)\left(\frac{\pi}{a}\right)^2 - (\gamma_1 + \gamma_2 + \alpha\gamma_3)(k_{x_1}^2 + k_{y_1}^2) + \frac{2\gamma_3\sqrt{3}d\varepsilon_{x_1y_1}}{\gamma_2(\pi/a)^2}k_{x_1}k_{y_1}, \quad (4.2)$$

where the numerical coefficient  $\alpha$  is defined by constants  $\gamma_1, \gamma_2, \gamma_3$  [61]; in our samples  $\alpha \simeq 0.4$ . The presence of heteroboundary with low symmetry also results in a similar mass anisotropy. As shown by Aleiner [62], the lowered symmetry of the heteroboundary at  $z_1 = z_\alpha$  is described by the Hamiltonian  $\mathcal{H}_{adm} = \frac{Va_0}{\sqrt{3}}[J_{x_1}J_{y_1}]\delta(z_1 - z_\alpha)$ , reflecting an admixture of heavy and light holes, where  $a_0$  is the lattice constant. In the presence of both strain and such admixture the spectrum is given by Eq. (4.2) with  $Va_0/2a$  added to  $d\varepsilon_{x_1y_1}$ . However, estimates show that strain-related anisotropy is the principal cause of anisotropy. It is also noteworthy that if the external strain is not purely shear strain, and  $\varepsilon_{x_1x_1} \neq \varepsilon_{y_1y_1}$ , then one more anisotropic term appears in Eq. (4.2), given by

$$\delta E = \frac{3b(\varepsilon_{x_1x_1} - \varepsilon_{y_1y_1})}{2(\pi/a)^2}(k_{x_1}^2 - k_{y_1}^2). \quad (4.3)$$

Then the direction of principal axes of reciprocal mass tensor, and, therefore, principal axes of the coefficients characterizing exchange energy, becomes dependent on the ratio of  $\varepsilon_{x_1y_1}$  and  $(\varepsilon_{x_1x_1} - \varepsilon_{y_1y_1})$ . However, in the present experiments  $\varepsilon_{x_1y_1}$  is predominant and thus the term  $(\varepsilon_{x_1x_1} - \varepsilon_{y_1y_1})$  is neglected, Eq. (4.2) is used for the 2D hole spectrum.

Switching to rotated axes  $x \rightarrow (x_1 + y_1)/\sqrt{2}$  and  $y \rightarrow (x_1 - y_1)/\sqrt{2}$  along  $[110]$  and  $[\bar{1}\bar{1}0]$ , the effective 2D charge carrier single-particle Hamiltonian in magnetic field  $\mathbf{H} = \nabla \times \mathbf{A}$  can be written as  $\mathcal{H}_{2D} = \mathcal{H}^\varepsilon + \mathcal{H}_4^{an}$ , where

$$\mathcal{H}^\varepsilon = \frac{(p_x - \frac{e}{c}A_x)^2}{2m_x} + \frac{(p_y - \frac{e}{c}A_x)^2}{2m_y}, \quad (4.4)$$

includes parabolic and  $\mathcal{H}_4^{an}$  includes higher order terms.

Here the mass in  $x$ -direction  $[110]$  is different from that in  $y$ -direction  $[\bar{1}\bar{1}0]$ , with  $m^{-1} = (m_x^{-1} + m_y^{-1})/2$  and  $\mu^{-1} = (m_x^{-1} - m_y^{-1})/2$  being the isotropic and anisotropic parts respectively. For holes quantized along the  $(001)$  direction  $m^{-1} = -(\gamma_1 + \gamma_2 + \alpha\gamma_3)/m_0$ , where  $\gamma_1, \gamma_2, \gamma_3$  are negative constants defining the bulk hole spectra and include the effects of spin-orbit coupling. The coefficient  $\alpha$  is defined by these constants [61]. The anisotropic part induced by the shear strain  $\varepsilon = \varepsilon_{xx} = -\varepsilon_{yy}$  is

$$\mu^{-1} = \gamma_3 \sqrt{3} d\varepsilon / [\gamma_2 (\pi \hbar / a)^2]$$

where  $d$  is the deformation potential [59], and  $a$  is the quantum well width. For electrons,  $m$  is the 3D effective electron mass  $m_c$ , while the anisotropic part, obtained in the third-order perturbation theory, is  $\hbar^2/2\mu = -P^2 d\varepsilon / \sqrt{3} E_g^2$ , where  $P$  is the Kane band coupling parameter [63] and  $E_g$  is the band gap. Note that the sign of the strain-induced term for electrons is opposite compared to that for holes. Anisotropic higher order terms  $\mathcal{H}_4^{an}$  do not break  $C_4$  symmetry and do not result in the inequivalence of  $[110]$  and  $[\bar{1}\bar{1}0]$  directions. Thus, it is instructive to consider the parabolic part separately and add strain-independent anisotropy using perturbation theory to final results. In the quartic approximation

$$\mathcal{H}_4^{an} = \beta p_x^2 p_y^2$$

where  $\beta = 3(\gamma_3^2 - \gamma_2^2)a^2 / (\pi^2 2m_0 \gamma_2 \hbar^2)$  for holes in the perturbative expansion.

To find the single particle wavefunctions of the 2D charge carriers in quantizing magnetic field  $H \parallel \hat{z}$ , the deformed coordinate system,  $x' = x\sqrt{\frac{m_x}{m}}$ ,  $y' = y\sqrt{\frac{m_y}{m}}$  is defined, where  $m = \sqrt{m_x m_y}$ . The single-particle Hamiltonian in the deformed

coordinate system is isotropic,  $\mathcal{H}_{2D} = \frac{(\mathbf{p}' - \frac{e}{c}\mathbf{A}')^2}{2m}$ , and the wavefunctions in deformed variables are the usual Landau level wavefunctions with degeneracy in guiding center coordinate quantum number  $X' = k'_y l^2$ , where  $l = \sqrt{\frac{\hbar c}{eH}}$  is the magnetic length. The following analysis that considers interacting electrons of partially filled high Landau level is done in the deformed co-ordinate system. This work shows that there exists a preferential crystallographic direction, in which the guiding center density wave develops at around half-filling of the highest occupied Landau level.

The physical picture developed by Aleiner and Glazman [58] looks at the properties of the 2D system with partially filled topmost Landau level, i.e., with one or several fully occupied Landau levels and partially filled  $N$ -th Landau level, as defined by Coulomb interactions of charge carriers of partially filled level, but with dielectric constant defined by the charge carriers of fully filled Landau levels. Thus, at  $N \gg r_s^{-1} \gg 1$ , i.e., at sufficiently large  $N$  and small  $r_s = \frac{1}{\pi n a_B^2}$ , where  $n$  is the 2D carrier density and  $a_B = \frac{\hbar^2}{me^2}$  is the Bohr radius, the low energy physics of the 2D electron liquid in weak magnetic field in the partially filled Landau level is described by the effective Hamiltonian

$$\mathcal{H}_{eff} = \frac{1}{L_x L_y} \sum_{\mathbf{q}'} \rho(\mathbf{q}') v(\mathbf{q}') \rho(-\mathbf{q}'), \quad (4.5)$$

where  $\rho(\mathbf{q}')$  is the projection of the density operator on the upper Landau level, and

$$v(\mathbf{q}') = \frac{2\pi e^2}{\kappa_0 \kappa(\mathbf{q}') \sqrt{(q'_x)^2 \frac{m_x}{m} + (q'_y)^2 \frac{m_y}{m}}} \quad (4.6)$$

is the Fourier component of renormalized electron-electron interaction potential in deformed coordinate system,  $\kappa_0$  is the background dielectric constant,  $\kappa(\mathbf{q}')$  is the effective dielectric constant. It is worthwhile to note that while the single-particle Hamiltonian is isotropic in deformed variables, the Coulomb potential is isotropic in physical (untransformed) variables. The quantity under the square root in  $v(\mathbf{q}')$  is in fact  $q = \sqrt{q_x^2 + q_y^2}$ , anisotropic in transformed variables but isotropic in physical ones. The effective dielectric constant for our system is given by

$$\kappa(\mathbf{q}') = 1 - \frac{2\pi e^2}{\kappa_0 q} \Pi(\mathbf{q}'), \quad (4.7)$$

where  $\Pi(\mathbf{q}')$  is the polarization operator isotropic in deformed variables. Furthermore,

$$\Pi(\mathbf{q}') = -\frac{m}{\pi\hbar^2}[1 - J_0^2(R_c q')] \quad (4.8)$$

where  $J_0(x)$  is the Bessel function,  $R_c = \sqrt{S/\pi}$  is the geometric average of the radii of the cyclotron ellipse,  $S$  is the area enclosed by the cyclotron ellipse. At  $R_c^{-1} \ll q' \ll k_F$ , where the Fermi wavevector is given by  $k_F = \sqrt{2mE_F}/\hbar$ ,  $E_F$  is the Fermi energy, the effective dielectric constant reduces to one obtained by Kukusknin *et al* [64]

$$\kappa(\mathbf{q}') = 1 + \frac{2}{qa_B}, \quad (4.9)$$

and is isotropic in physical (as opposed to deformed) space. The Fourier-component of the charge density operator is given by

$$\rho(\mathbf{q}') = \sum_{X'} \alpha_N(\mathbf{q}') e^{-iq'_x(X' - q'_y l^2/2)} a_{X'}^\dagger a_{X' - q'_y l^2}, \quad (4.10)$$

where  $\alpha_N(\mathbf{q}') = L_N^0(\frac{\mathbf{q}'^2 l^2}{2}) \exp(-\frac{\mathbf{q}'^2 l^2}{4})$ ,  $L_N^0(x)$  is the Laguerre polynomial, and  $a_{X'}^\dagger$  ( $a_{X'}$ ) is the creation (annihilation) operator for a hole with guiding center at  $X'$  in the topmost LL. Defining the CDW order parameter  $\Delta(\mathbf{q}') = \frac{2\pi l^2}{L_x L_y} \sum_{X'} a_{X' + q'_y l^2/2}^\dagger a_{X' - q'_y l^2/2}$ , the Hartree-Fock energy is obtained to be

$$E_{HF} = \frac{1}{2\pi l^2 \nu_N} \sum_{\mathbf{q}' \neq 0} [u_H(\mathbf{q}') - u_{ex}(\mathbf{q}')] \Delta(\mathbf{q}') \Delta(-\mathbf{q}'), \quad (4.11)$$

where  $0 \leq \nu_N \leq 1$  is the filling of the topmost LL and the Hartree-Fock potential as :

$$H_{HF}^{eff} = \sum_{X'} a_{X' - \frac{q'_y l^2}{2}}^\dagger a_{X' + \frac{q'_y l^2}{2}} e^{iQ'_x X'} \Delta(\mathbf{Q}') \times [u_H(\mathbf{Q}') - u_{ex}(\mathbf{Q}')], \quad (4.12)$$

The Fourier transforms of the Hartree and exchange potentials are, respectively,  $u_H(\mathbf{q}') = v(\mathbf{q}')[\alpha_N(\mathbf{q}')]^2$  and

$$u_{ex}(\mathbf{q}') = \frac{2\pi l^2}{L_x L_y} \sum_{\mathbf{Q}'} u_H(\mathbf{Q}') \exp[il^2(-Q'_x q'_y + Q'_y q'_x)]. \quad (4.13)$$

Note that the two potentials are related by a Fourier transform but the arguments in the Fourier transform of the Hartree potential are transposed relative to the arguments of  $u_{ex}$ . While this transposition is not important in the isotropic case [18],

taking it into account here is crucial for finding the preferred orientation of the CDW modulation.

Applying an analysis similar to that in [18], it can be seen that when the Laguerre polynomial in  $\alpha_n(\mathbf{Q}')$  is zero and the Hartree term is zero, the total Hartree-Fock energy is negative and is given by the exchange contribution. The system is then unstable with respect to the formation of the “guiding center” density wave with the wavevector close to  $\mathbf{Q}'$ . However, in contrast to isotropic system, in which any direction of  $\mathbf{Q}'$  and  $\mathbf{Q}$  gives the same magnitude of energy, so that the direction of the charge density wave has to be chosen spontaneously, in our case the smallest  $\mathbf{Q}'$ , which corresponds to the direction with larger mass gives the largest value of the exchange and the lowest HF energy. This can be seen, by expanding Eq. (4.12) in small anisotropy parameter  $\delta m/m_s$ , where  $m_s = (m_x + m_y)/2$ . The leading term in the Fourier-component of the exchange interaction is then isotropic in the deformed coordinate system, and is given by

$$-\frac{2\pi l^2}{L_x L_y} \sum_{\mathbf{q}'} [\alpha_N(\mathbf{q}')]^2 \times \frac{e^2}{q' \sqrt{\frac{m_s}{m}} + 2a_B^{-1}} e^{i l^2 (-q'_x Q'_y + q'_y Q'_x)}, \quad (4.14)$$

where  $q' = \sqrt{q_x'^2 + q_y'^2}$ . This term gives the same Hartree-Fock potential for any orientation of the charge density wave wavevector  $\mathbf{Q}'$  (and therefore corresponding  $\mathbf{Q}$ ), so that there is no preferential direction of anisotropy. The anisotropic term which determines the preferential direction is

$$-\frac{\delta m}{2\sqrt{m_s m}} \frac{2\pi l^2}{L_x L_y} \sum_{\mathbf{q}'} [\alpha_N(\mathbf{q}')]^2 \times \frac{e^2 (q_y'^2 - q_x'^2)}{q' (q' \sqrt{\frac{m_s}{m}} + 2a_B^{-1})^2} e^{i l^2 (-q'_x Q'_y + q'_y Q'_x)}, \quad (4.15)$$

Two-dimensional integrals in Eqs.(4.14) and (4.15) after switching to polar coordinates are easily reduced to integrals over absolute value of  $q'$ , with kernel arising from (4.14) expressed via Bessel function  $J_0(q'Q')$  and kernel arising from (4.15) expressed via  $J_2(q'Q')$ . The remaining integrals are evaluated numerically and the ratio of isotropic and anisotropic parts of the exchange energy (including the higher order anisotropic terms  $\mathcal{H}_4^{an}$ ) is plotted in Fig. 4.4 for positive and negative shear strains. The constants used in the calculations are  $d = -5.4eV$ ,  $\gamma_1 = -6.8$ ,  $\gamma_2 = -2.4$ ,

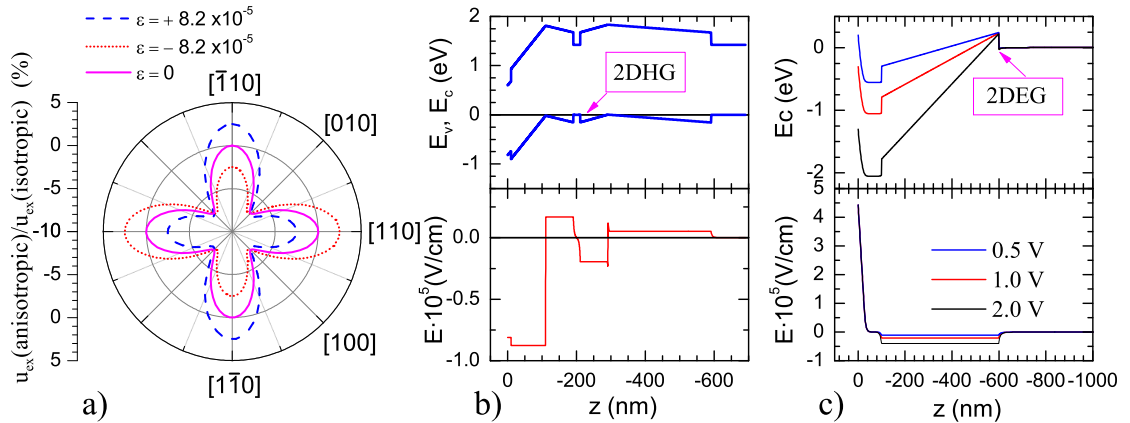


Figure 4.4. a) The ratio of isotropic and anisotropic parts of the hole exchange potential for three values of shear strain  $\varepsilon$ . Strain-dependent (Eq. 4.13) and strain-independent quartic corrections to the exchange are included. b) Self-consistent calculations of the band profile and internal electric fields in the studied wafer. c) Modeling of a HIGFET structure from [65].

$\gamma_3 = -2.9$ , and  $\alpha = -0.4$ . Note that the difference in exchange energy between CDW in  $[110]$  or in  $[1\bar{1}0]$  directions reaches 5% for strains of  $10^{-4}$ . The CDW near the half filling of the  $N$ -th LL naturally results in stripes with alternating  $\nu_N = 0$  and  $\nu_N = 1$ , which, in turn, translates into low resistance direction along the stripes and high resistance direction perpendicular to the stripes. Thus, in the presence of  $\varepsilon \neq 0$ , the CDW has a preferential direction defined by the sign of the strain, consistent with the experimental results. While the theory is valid, strictly speaking, in high Landau levels it appears to describe experiments even at  $N = 1$ , the lowest LL for which  $L_N^0(x)$  has a zero.

#### 4.5 Internal strain in GaAs/AlGaAs heterostructure caused by built in electric field

The preceding analysis suggests that internal strain may be responsible for the observed orientation of stripes in externally unstrained samples. GaAs is a piezoelectric material and any electric field in the  $\hat{z}$  direction results in an in-plane shear strain  $\varepsilon = d_{14}E_z$ , where  $d_{14} = -2.7 \cdot 10^{-10}$  cm/V. A calculated band diagram for our samples is shown in Fig. 4.4b. Inside the QW  $E_z < 2 \cdot 10^4$  V/cm and results in strain too small to orient the stripes.  $E_z$  on both sides of the QW, caused by doping, is also small and, in our samples, odd in  $z$ . However, in all GaAs samples there is a large field near the surface of the wafer due to the pinning of the Fermi energy near mid-gap. This surface charge-induced field is  $\sim -10^6$  V/cm and the corresponding strain is  $\varepsilon \sim 3 \cdot 10^{-5}$ . If transmitted to the QW region, this strain has the correct sign and magnitude to explain the observed orientation of stripes in externally unstrained samples. To show that transmission of strain does indeed occur, a minimal model in which this effect is present is considered. The following theory was developed by Prof. Sergei Khlebnikov. The free energy of the model is given by

$$\mathcal{F}_{\text{el}} = \frac{1}{2}\lambda [(\partial_x u_y + \partial_y u_x)^2 + (\partial_z u_x)^2 + (\partial_z u_y)^2] ,$$

where  $u_x$  and  $u_y$  denote displacements, and  $x, y, z$  correspond to the [100], [010], [001] directions, respectively. The total free energy density, including that due to the electric field  $\mathbf{E} = -\nabla\Phi$ , is

$$\mathcal{F} = \mathcal{F}_{\text{el}} + \frac{1}{2}\kappa\mathbf{E}^2 + 2\beta E_z \varepsilon_{xy} + \Phi\rho_{\text{ext}} ,$$

where  $\varepsilon_{xy} = \frac{1}{2}(\partial_x u_y + \partial_y u_x)$  is the strain, and  $\rho_{\text{ext}}$  is the density of external charges. The model free energy thus involves three constants: the elastic constant  $\lambda$ , the dielectric constant  $\kappa$ , and the piezoelectric constant  $\beta$ .

The elastic equilibrium equations corresponding to this free energy are

$$\begin{aligned} 2\partial_y \varepsilon_{xy} + \partial_z^2 u_x + \tilde{\beta}\partial_y E_z &= 0 \\ 2\partial_x \varepsilon_{yx} + \partial_z^2 u_y + \tilde{\beta}\partial_x E_z &= 0 , \end{aligned}$$

where  $\tilde{\beta} = \beta/\lambda$ . The relevant case is when the field  $E_z$  has no uniform component with respect to  $z$ :

$$\int_0^d E_z(x, y, z) dz = 0 ,$$

where  $d$  is the total thickness of the sample. Within our model, bulk strain can then exist only if the field is nonuniform with respect to  $x$  and  $y$ , which is true in realistic devices, where  $E_z(x, y, z)$  is nonuniform in  $(x, y)$  plane due to charge fluctuations on the surface and in the doping layer.

For illustration, consider a field that has cylindrical symmetry:  $E_z(x, y, z) = E_z(r, z)$ . In this case, the equilibrium equations have a solution of the form

$$\begin{aligned} u_x(r, \phi, z) &= U(r, z) \sin \phi , \\ u_y(r, \phi, z) &= U(r, z) \cos \phi , \end{aligned}$$

where  $U(r, z)$  is a single function of two variables which satisfies the equation

$$\partial_r \left[ \frac{1}{r} \partial_r (rU) \right] + \partial_z^2 U = -\tilde{\beta} \partial_r E_z .$$

Expanding  $U$  and  $E_z$  in Bessel functions, as follows:

$$\begin{aligned} E_z(r, z) &= \sum_n E_n(z) J_0(q_n r) , \\ U(r, z) &= \sum_n U_n(z) J_1(q_n r) , \end{aligned}$$

the equations for the individual components are obtained to be,

$$(\partial_z^2 - q_n^2) U_n(z) = \tilde{\beta} q_n E_n(z) . \quad (4.16)$$

The boundary conditions at  $z = 0$  and  $d$  are  $\partial_z U_n = 0$ . The solution of strain is then,

$$\varepsilon_{xy}(r, z) = \frac{\beta}{2\lambda} \sum_n \frac{q_n^2}{\partial_z^2 - q_n^2} E_n(z) J_0(q_n r) + \varepsilon_b(r, z) , \quad (4.17)$$

where  $\varepsilon_b$  is localized near  $r = L$ . If  $E_z(r, z)$  varies with  $r$  at some characteristic scale  $R$ , a typical  $q_n$  is of order  $1/R$ . Then, according to Eq. 4.17, the corresponding component of the strain propagates largely undiminished over distances  $z \sim R$  from

the region where  $E_n(z)$  is large (sample surface). As a result, macroscopic regions with sizable strain exist throughout the QW region.

The picture of internal strain allows us to explain orientation of stripes found in 2D electron gases. A typical band diagram of an electron sample is similar to that shown in Fig. 4.4b, but is inverted relative to the Fermi level with both the surface electric field and the shear strain changing sign. However, the anisotropic term in Eq. 4.4 also has opposite sign for electrons and holes, so that the sign of the anisotropic term in electron and hole exchange is the same. Thus, for both holes and electrons, a surface field will orient the CDW along [110], as seen in experiments. With the model developed above, the reorientation of stripes as a function of density observed in a HIGFET (Heterojunction-Insulated Gate Field Effect Transistor) [65] can also be explained. At low gate voltages (low densities), shear strain will be dominated by the surface field, see Fig. 4.4c. At large gate voltages (2 V corresponds to  $3 \cdot 10^{11} \text{ cm}^{-2}$ ), the electric field across the AlGaAs barrier becomes large enough to change the sign of the strain in the 2D gas region, thus reorienting the stripes.

## 4.6 Conclusion

In summary, we have shown experimentally that orientation of CDW in the QH regime can be controlled by external strain. Theoretically, this effect has been traced to a strain-induced anisotropy of the exchange interaction and a competition between the internal and external strain. In general, any factor that brings in a crystallographic anisotropy of spectrum gives rise to a crystallographic anisotropy of the Hartree-Fock energy of the CDW state (this is the case, for example, in hole gases grown on low-symmetry (311) GaAs [23]). The theory developed as part of this work includes calculations of the effect of quartic anisotropy of spectrum on exchange potential and shows that the directions 001 and 010 become unfavorable, while directions [110] and  $[1\bar{1}0]$  become favorable for the propagation of CDW. However the most important effect arises because of strain, and in heterostructures grown in the

high-symmetry (001) surfaces, piezoelectricity due to surface electric fields becomes the source of inequivalence of  $[110]$  and  $[\bar{1}\bar{1}0]$  directions for CDW propagation. We underscore that, although the anisotropy of electron Hartree-Fock energy is two orders of magnitude smaller than that for holes, it must still choose a preferential direction for the CDW of guiding centers. Therefore, the preferential direction of the resistance anisotropy in (001) samples appears to be universally dictated by internal strain.

## LIST OF REFERENCES

## LIST OF REFERENCES

- [1] J. Bardeen and W.H. Brattain. The transistor, a semi-conductor triode. *Physical Review*, 74:230 – 231, 1948/07/15.
- [2] G. Binasch, P. Grünberg, F. Saurenbach, and W. Zinn. Enhanced magnetoresistance in layered magnetic structures with antiferromagnetic interlayer exchange. *Phys. Rev. B*, 39(7):4828–4830, Mar 1989.
- [3] M.N. Baibich, J.M. Broto, A. Fert, F. Nguyen Van Dau, F. Petroff, P. Etienne, G. Creuzet, A. Friederich, and J. Chazelas. Giant magnetoresistance of (001)fe/(001)cr magnetic superlattices. *Phys. Rev. Lett.*, 61(21):2472, 1988.
- [4] S. Datta and B. Das. *Applied Physics Letters*, 56(7):665 – 7, 1990/02/12.
- [5] S. Y. Lin, H. P. Wei, D. C. Tsui, J. F. Klem, and S. J. Allen. *Phys. Rev. B*, 43(14):12110–12113, May 1991.
- [6] Maryam Rahimi, M. R. Sakr, S. V. Kravchenko, S. C. Dultz, and H. W. Jiang. *Phys. Rev. B*, 67:081302(R), 2003.
- [7] S. J. Papadakis, E. P. De Poortere, M. Shayegan, and R. Winkler. *Phys. Rev. Lett.*, 84(24):5592 – 5595, 2000.
- [8] R. Winkler, S.J. Papadakis, E.P. De Poortere, and M. Shayegan. *Physical Review Letters*, 85(21):4574 – 7, 2000/11/20.
- [9] B. J. van Wees, H. van Houten, C. W. J. Beenakker, J. G. Williamson, L. P. Kouwenhoven, D. van der Marel, and C. T. Foxon. *Phys. Rev. Lett.*, 60:848, 1988.
- [10] D. A. Wharam, T. J. Thornton, R. Newbury, M. Pepper, H. Ahmed, J. E. F. Frost, D. G. Hasko, D. C. Peacock, D. A. Ritchie, and G. A. C. Jones. *J. Phys. C*, 21:L209–214, 1988.
- [11] R. Landauer. *IBM J. Res. Dev. (USA)*, 32(3):306 – 16, 1988/05/.
- [12] M. Buttiker. *IBM J. Res. Dev. (USA)*, 32(3):317 – 34, 1988/05/.
- [13] I. Zailer, J. E. F. Frost, C. J. B. Ford, M. Pepper, M. Y. Simmons, D. A. Ritchie, J. T. Nicholls, and G. A. C. Jones. *Phys. Rev. B*, 49(7):5101–5104, 1994.
- [14] A. J. Daneshvar, C. J. B. Ford, A. R. Hamilton, M. Y. Simmons, M. Pepper, and D. A. Ritchie. *Phys. Rev. B*, 55(20):R13409–R13412, 1997.
- [15] L. P. Rokhinson, D. C. Tsui, L. N. Pfeiffer, and K. W. West. *Superlattices Microstruct.*, 32:99–102, 2002.
- [16] R. B. Laughlin. *Phys. Rev. Lett.*, 50:1395, 1983.

- [17] H. Fukuyama, P. M. Platzman, and P. W. Anderson. Two-dimensional electron gas in a strong magnetic field. *Phys. Rev. B*, 19(10):5211–5217, May 1979.
- [18] M.M. Fogler, A.A. Koulakov, and B.I. Shklovskii. Ground state of a two-dimensional electron liquid in a weak magnetic field. *Physical Review B (Condensed Matter)*, 54(3):1853 – 71, 1996/07/15.
- [19] A.A. Koulakov, M.M. Fogler, and B.I. Shklovskii. Charge density wave in two-dimensional electron liquid in weak magnetic field. *Physical Review Letters*, 76(3):499 –, 1996.
- [20] R. Moessner and J. T. Chalker. Exact results for interacting electrons in high Landau levels. *Phys. Rev. B*, 54(7):5006–5015, Aug 1996.
- [21] M.P. Lilly, K.B. Cooper, J.P. Eisenstein, L.N. Pfeiffer, and K.W. West. *Physical Review Letters*, 82(2):394 –, 1999.
- [22] R.R. Du, W. Pan, H.L. Stormer, D.C. Tsui, L.N. Pfeiffer, K.W. Baldwin, and K.W. West. *Physica E: Low-Dimensional Systems and Nanostructures*, 6(1):36 – 39, 2000.
- [23] M. Shayegan, H. C. Manoharan, S. J. Papadakis, and E. P. De Poortere. Anisotropic transport of two-dimensional holes in high Landau levels. *Physica E*, 6:40 – 42, 2000.
- [24] M.J. Manfra, R. De Picciotto, Z. Jiang, S.H. Simon, L.N. Pfeiffer, K.W. West, and A.M. Sergent. *Physical Review Letters*, 98(20):206804 –, 2007.
- [25] J.P. Eisenstein. Two-dimensional electrons in excited Landau levels: evidence for new collective states. *Solid State Communications*, 117(3):123 – 131, 2001.
- [26] R.K. Hayden, E.C. Valadares, M. Henini, L. Eaves, D.K. Maude, and J.C. Portal. *Phys. Rev. B, Condens. Matter (USA)*, 46(23):15586 – 9, 1992/12/15.
- [27] J.J. Heremans, M.B. Santos, K. Hirakawa, and M. Shayegan. *J. Appl. Phys.*, 76(3):1980 – 2, 1994.
- [28] R. Held, T. Vancura, T. Heinzel, K. Ensslin, M. Holland, and W. Wegscheider. *Applied Physics Letters*, 73(2):262 –, 1998.
- [29] M.Y. Simmons, A.R. Hamilton, S.J. Stevens, D.A. Ritchie, M. Pepper, and A. Kurobe. *Appl. Phys. Lett. (USA)*, 70(20):2750 – 2, 1997/05/19.
- [30] M.J. Manfra, L.N. Pfeiffer, K.W. West, R. de Picciotto, and K.W. Baldwin. *Appl. Phys. Lett. (USA)*, 86(16):162106 – 1, 2005/04/18.
- [31] R. Held, T. Heinzel, P. Studerus, K. Ensslin, and M. Holland. *Applied Physics Letters*, 71(18):2689–2691, 1997.
- [32] E. S. Snow and P. M. Campbell. *Science*, 270:1639, 1995.
- [33] R.E. Held. PhD thesis, 2000.
- [34] Veeco Scanning Probe Microscopy, Training Notebook.

- [35] D. Graf, M. Frommenwiler, P. Studerus, T. Ihn, K. Ensslin, D.C. Driscoll, and A.C. Gossard. *Journal of Applied Physics*, 99(5):053707 –, 2006.
- [36] R. Winkler. volume 191 of *Springer Tracts in Modern Physics*. Springer Berlin / Heidelberg, 2003.
- [37] R. Danneau, O. Klochan, W.R. Clarke, L.H. Ho, A.P. Micolich, M.Y. Simmons, A.R. Hamilton, M. Pepper, D.A. Ritchie, and U. Zulicke. *Phys. Rev. Lett.*, 97(2):026403 – 1, 2006.
- [38] K. J. Thomas, J. T. Nicholls, M. Y. Simmons, M. Pepper, D. R. Mace, and D. A. Ritchie. *Phys. Rev. Lett.*, 77:135–138, 1996.
- [39] A. C. Graham, K. J. Thomas, M. Pepper, N. R. Cooper, M. Y. Simmons, and D. A. Ritchie. *Phys. Rev. Lett.*, 91(13):136404, Sep 2003.
- [40] L. I. Glazman and A. V. Khaetskii. Nonlinear quantum conductance of a lateral microconstraint in a heterostructure. *EPL (Europhysics Letters)*, 9(3):263, 1989.
- [41] N K Patel, L Martin-Moreno, M Pepper, R Newbury, J E F Frost, D A Ritchie, G A C Jones, J T M B Janssen, J Singleton, and J A A J Perenboom. Ballistic transport in one dimension: additional quantisation produced by an electric field. *Journal of Physics: Condensed Matter*, 2(34):7247, 1990.
- [42] N. K. Patel, J. T. Nicholls, L. Martn-Moreno, M. Pepper, J. E. F. Frost, D. A. Ritchie, and G. A. C. Jones. Evolution of half plateaus as a function of electric field in a ballistic quasi-one-dimensional constriction. *Phys. Rev. B*, 44(24):13549–13555, Dec 1991.
- [43] G. Salis, T. Heinzel, K. Ensslin, O. J. Homan, W. Bächtold, K. Maranowski, and A. C. Gossard. *Phys. Rev. B*, 60(11):7756–7759, Sep 1999.
- [44] H. Kroemer. On the magnetoresistance anisotropy of a 2-dimensional electron gas with large half-integer filling factors. *cond-mat/9901016*, 1999.
- [45] E. E. Takhtamirov and V. A. Volkov. Orientational pinning of the striped phase in a quantum Hall liquid. *JETP Lett.*, 71:422–425, 2000.
- [46] B. Rosenow and S. Stefan. Quantum Hall stripes: Chern-Simons theory and orientational mechanisms. *International Journal of Modern Physics B*, 15(13):1905–1914, 2001.
- [47] M. M. Fogler. *High Magnetic Fields: Applications in Condensed Matter Physics and Spectroscopy*, volume 595 of *Lect. Notes Phys.* Springer, Berlin, 2002.
- [48] K. B. Cooper, M. P. Lilly, J. P. Eisenstein, T. Jungwirth, L. N. Pfeiffer, and K. W. West. An investigation of orientational symmetry-breaking mechanisms in high Landau levels. *Sol. Stat. Comm.*, 119(2):89 – 94, 2001.
- [49] E. I. Rashba and E. Ya. Sherman. Anisotropic electron-electron interaction via piezophonons and its influence on the formation of electronic phases. *Sov. Phys. Semicond.*, 21:1185–1187, 1987.
- [50] E. Ya. Sherman. Angular pinning and domain structure of a two-dimensional Wigner crystal in a III-V semiconductor. *Phys. Rev. B*, 52:1512–1515, 1995.

- [51] D. V. Fil. Piezoelectric mechanism for the orientation of stripe structures in two-dimensional electron systems. *Low Temp. Phys.*, 26:581 – 5, 2000.
- [52] W. Pan, R.R. Du, H.L. Stormer, D.C. Tsui, L.N. Pfeiffer, K.W. Baldwin, and K.W. West. *Physical Review Letters*, 83(4):820 –, 1999.
- [53] M. P. Lilly, K. B. Cooper, J. P. Eisenstein, L. N. Pfeiffer, and K. W. West. Anisotropic states of two-dimensional electron systems in high Landau levels: Effect of an in-plane magnetic field. *Phys. Rev. Lett.*, 83:824 – 7, 1999.
- [54] T. Jungwirth, A. H. MacDonald, L. Smrčka, and S. M. Girvin. Field-tilt anisotropy energy in quantum Hall stripe states. *Phys. Rev. B*, 60:15574–15577, 1999.
- [55] Tudor D. Stanescu, Ivar Martin, and Philip Phillips. Finite-temperature density instability at high Landau level occupancy. *Phys. Rev. Lett.*, 84:1288–1291, 2000.
- [56] M. Shayegan, K. Karrai, Y.P. Shkolnikov, K. Vakili, E.P. De Poortere, and S. Manus. *Applied Physics Letters*, 83(25):5235 – 7, 2003/12/22.
- [57] A. K. Fung, L. Cong, J. D. Albrecht, M. I. Nathan, P. P. Ruden, and H. Shtrikman. Linear in-plane uniaxial stress effects on the device characteristics of Al-GaAs/GaAs modulation doped field effect transistors. *J Appl. Phys.*, 81:502–505, 1997.
- [58] I. L. Aleiner and L. I. Glazman. Two-dimensional electron liquid in a weak magnetic field. *Phys. Rev. B*, 52(15):11296–11312, Oct 1995.
- [59] G. L. Bir and G. E. Pikus. *Symmetry and strain-induced effects in semiconductors*. Wiley, New York, 1974.
- [60] J. M. Luttinger. Quantum theory of cyclotron resonance in semiconductors: General theory. *Phys. Rev.*, 102(4):1030–1041, May 1956.
- [61] S. S. Nedorezov. Space quantization in semiconductor films. *Soviet Physics–Solid State*, 12(8):1814–1819, 1971.
- [62] I. L. Aleiner and E.L. Ivchenko. Anisotropic exchange splitting in type-II GaAs/AlAs superlattices. *JETP Lett.*, 55:692–695, 1992.
- [63] E. O. Kane. Band structure of indium antimonide. *Journal of Physics and Chemistry of Solids*, 1:249–261, 1957.
- [64] I. V. Kukushkin, S. V. Meshkov, and V. B. Timofeyev. Two-dimensional electron density of states in a transverse magnetic field. *Uspehi Fiz. Nauk*, 155:219–264, 1988.
- [65] J. Zhu, W. Pan, H. L. Stormer, L. N. Pfeiffer, and K. W. West. Density-induced interchange of anisotropy axes at half-filled high Landau levels. *Phys. Rev. Lett.*, 88:116803, 2002.

VITA

## VITA

**EDUCATION**

**Ph.D**, Physics (Experimental Condensed Matter)

Purdue University, West Lafayette, IN 47907, December 2010

**Master of Science**, Physics

Indian Institute of Technology(IIT), Madras, India, 2003

**Bachelor of Science**, Physics

Madras Christian College, Madras, India, 2001

**EXPERIMENTAL****SKILLS****AND TRAINING**

- Lithography:

  - Photolithography

  - e-beam lithography

  - AFM lithography using Local Anodic Oxidation

- Etching

  - Dry etching : XeF<sub>2</sub> etcher, Plasma Reactive Ion Etching techniques (RIE)

  - Wet etching techniques for GaAs, Si/SiGe etc

- Metallization:

  - Thermal evaporation: Denton, Edwards systems

  - e-beam evaporation: Airco, CHA

- Imaging: AFM, SEM

- Trained in various low temperature, low noise measurement and high vacuum techniques
- Trained for ISO Class 3 cleanroom
- Machine shop techniques
- Transport measurements using Oxford Dilution Refrigerator and He 3 Refrigerator

## PUBLICATIONS

- Sunanda P Koduvayur, Leonid P Rokhinson, Daniel C Tsui, L.N.Pfeiffer, K.W.West, “Anisotropic modification of effective hole  $g$ -factor by electrostatic confinement” Physical Review Letters **100**, 126401, 2008 (<http://arxiv.org/abs/0802.4271>)
- Pranawa C Deshmukh, Tanima Banerjee, Sunanda P Koduvayur, Hari R Verma “Interchannel coupling effects on non-dipole photoionization parameters.” Radiation Physics and Chemistry, Vol.75 Issue 12,pp 2211-2220, 2006
- Effect of strain on nematic phases in two-dimensional holes (Submitted to Physical Review Letters)

## CONFERENCE PRESENTATIONS, INVITED TALKS AND POSTERS

- “Effect of strain on stripe phases in quantum Hall effect”, APS Condensed Matter Division March meeting, March 2010
- “Preferential orientation of stripes in high Landau levels”, APS Condensed Matter Division March meeting, March 2010
- “Spin-orbit interactions in two and one dimensional systems”, Portland Technology Development (PTD), Intel, OR, October 2009
- “Effect of strain on nematic phases of two dimensional hole gases”, accepted for poster presentation, Electronic Properties of Two Dimensional Systems (EP2DS), Kobe, Japan, July 2009

- “Effect of strain on nematic phases of two dimensional hole gases”, presentation, APS Condensed Matter Division March meeting, March 2009
- “g-factor anisotropy in p-type GaAs/AlGaAs quantum point contacts”, presentation, APS Condensed Matter Division March meeting, March 2006
- “Newly found dynamical effects on photoelectron parameters in the dipole approximation for atomic Xe”, Poster, XV National conference on Atomic and Molecular Physics, Physical Research Laboratory, Ahmedabad, India, December 2004

## WORKSHOPS

- Workshop on Silicon Qubit Quantum Information Science and Technology, Berkeley, California, August 2009
- Boulder summer school on “Physics of Mesoscopic systems”, University of Colorado, Boulder, July 2005
- Workshop on “Quantum Computation”, Institute of Mathematical Sciences, Madras, India, June, 2002
- Workshop on “Quantum Information and Entanglement”, Institute of Mathematical Sciences, Madras, India, June, 2002

## SOFTWARE SKILLS

C, C++, Labview, matlab, various lithography software

## WORK EXPERIENCE

- Research Assistant, Purdue University, 2005-2010
- Teaching Assistant, Purdue University, 2004-2005

- Project Associate, Atomic and Molecular Physics Laboratory, IIT Madras, 2003-2004.
- Summer Intern, Institute of Mathematical Sciences, Madras, 2002.

## **AWARDS AND HONORS**

- Lijuan Wang memorial award, Department of Physics, Purdue, 2010
- Women in Science Travel grant, Women in Science program at Purdue, 2009
- H.Y.Fan Award for outstanding research in Experimental Condensed Matter Physics, Purdue University, 2008
- Best Poster Award : XV National Conference on Atomic and Molecular Physics, Physical Research Laboratory, Ahmedabad, India, 2004
- Cited for Merit cum Means scholarship, IIT Madras, 2001
- Recipient of Buckle's studentship, Madras Christian College, 1998.
- Recipient of Director General's (of (1) TN Air Sqn National Cadet Corp) scholarship for academic excellence, Madras Christian College, 1999

## **EXTRA CURRICULAR ACTIVITIES**

- President, Asha for Education Purdue Chapter, 2006-2007
- Journalist, Science Fest(Shaastra-2001) magazine, 2001
- B certificate holder, National Cadet Corps, India, 2000
- Glider Pilot certification, India, 1999

## **REFERENCES**

Provided upon request